1 **Vehicle-based in-situ observations of the water vapor isotopic**

2 **composition across China: spatial and seasonal distributions and**

3 **controls**

4 Di Wang[1,2,3], Lide Tian[1, 3], Camille Risi[2], Xuejie Wang[1,3], Jiangpeng Cui[4], Gabriel J.

5 Bowen[5], Kei Yoshimura[6], Zhongwang Wei[7], Laurent Z.X Li[2]

6 *[1] Institute of International Rivers and Eco-security, Yunnan University, Kunming 650500,*

7 *Yunnan, China*

8 *[2] Laboratoire de Météorologie Dynamique, IPSL, CNRS, Sorbonne Université, Campus*

9 *Pierre et Marie Curie, Paris 75005, France*

10 *[3] Yunnan Key Laboratory of International Rivers and Transboundary Eco–security,*

11 *Kunming 650500, Yunnan, China*

12 *[4] Sino-French Institute for Earth System Science, College of Urban and Environmental*

13 *Sciences, Peking University, Beijing 100871, China*

14 *[5] Department of Geology and Geophysics, and Global Change and Sustainability Center,*

15 *University of Utah, Salt Lake City, Utah 84108, USA*

16 *[6] Institute of Industrial Science, The University of Tokyo, Tokyo113-8654, Japan*

17 *[7] School of Atmospheric Sciences, Sun Yat-sen University, Guangzhou 510275, Guangdong,*

18 *China*

19 *Corresponding author: wangdishi.mp@hotmail.com; ldtian@ynu.edu.cn.*

21   **Abstract**

22   Stable water isotopes are natural tracers in the hydrological cycle and have been applied
23   in hydrology, atmospheric science, ecology, and paleoclimatology. However, the factors
24   controlling the isotopic distribution, both at spatial and temporal scales, are debated in low and
25   middle latitudes regions, due to the significant influence of large-scale atmospheric circulation
26   and complex sources of water vapor. For the first time, we made in-situ observations of near-
27   surface vapor isotopes over a large region (over 10000 km) across China in both pre-monsoon
28   and monsoon seasons, using a newly-designed vehicle-based vapor isotope monitoring system.
29   Combined with daily and multi-year monthly mean outputs from the isotope-incorporated
30   global spectral model (Iso-GSM) and IASI satellite to calculate the relative contribution, we
31   found that the observed spatial variations in both periods represent mainly seasonal-mean
32   spatial variations, but are influenced by more significant synoptic-scale variations during the
33   monsoon period. The spatial variations of vapor $\delta^{18}O$ are mainly controlled by Rayleigh
34   distillation along air mass trajectories during the pre-monsoon period, but are significantly
35   influenced by different moisture sources, continental recycling processes and convection during
36   moisture transport in the monsoon period. Thus, the North-South gradient observed during the
37   pre-monsoon period is counteracted during the monsoon period. The seasonal variation of vapor
38      $\delta^{18}O$ reflects the influence of the summer monsoon convective precipitation in southern China,
39   and a dependence on temperature in the North. The spatial and seasonal variations in d-excess
40   reflect the different moisture sources and the influence of continental recycling. Iso-GSM
41   successfully captures the spatial distribution of vapor $\delta^{18}O$ during the pre-monsoon period, but
42   the performance is weaker during the monsoon period, maybe due to the underestimation of
43   local or short-term high-frequency synoptic variations. These results provide an overview of
44   the spatial distribution and seasonal variability of water isotopic composition in East Asia and
45   their controlling factors, and emphasize the need to interpret proxy records in the context of the
46   regional system.

47   **Keywords:** Vapor isotopes, Spatial distribution, Seasonal difference, East Asia, Moisture
48   sources, Moisture propagation

49

1. Introduction

Stable water isotopes have been applied to study a wide range of hydrological and climatic processes (Gat, 1996;Bowen et al., 2019;West et al., 2009). This is because water isotopes vary with the water phases (e.g., evaporation, condensation), and therefore produce a natural labeling effect within the global water cycle. Stable isotopic signals recorded in natural precipitation archives are used in the reconstructions of ancient continental climate and hydrological cycles due to their strong relationship with local meteorological conditions. Examples include ice cores (Thompson, 2000;Yao et al., 1991;Tian et al., 2006), tree-ring cellulose (Liu et al., 2017), stalagmites (Van Breukelen et al., 2008), and lake deposits (Hou et al., 2007). However, unlike in polar ice cores, isotopic records in ice cores from low and middle latitudes regions have encountered challenges as temperature proxies (Brown et al., 2006;Thompson et al., 1997).

East Asian country China is the main distribution areas of ice cores in the low and middle latitudes (Schneider and Noone, 2007). Where the interpretation of isotopic variations in natural precipitation archives are debated, because they can be interpreted as recording temperature (Thompson et al., 1993;Thompson et al., 1997;Thompson et al., 2000;Thompson, 2000), regional-scale rainfall or strength of the Indian monsoon (Pausata et al., 2011), origin of air masses (Aggarwal et al., 2004;Risi et al., 2010). This is because China has a typical monsoon climate and moisture from several sources mix in this region (Wang, 2002;Domrös and Peng, 2012). In general, large parts of the country are affected by the Indian monsoon and the East Asian monsoon in summer, which bring humid marine moisture from the Indian Ocean, South China Sea, and Northwestern Pacific Ocean (Fig.1). During the non-monsoon seasons, the Westerlies influence most of northern China (Fig.1). Westerlies brings extremely cold and dry air masses. Occasional moisture flow from the Indian Ocean and/or Pacific Ocean brings moisture to southern China. Continental recycling, i.e. the moistening of the near-surface air by the evapo-transpiration from the land surface (transpiration by plants, evaporation of bare soil or standing water bodies,(Brubaker et al., 1993)), is also an important source of water vapor in both seasons. Some of the spatial and seasonal patterns of water vapor transport are imprinted in the observed station-based precipitation isotopes (Araguás-Araguás et al., 1998;Tian et al., 2007;Wright, 1993;Mei'e et al., 1985;Tan, 2014). However, precipitation isotopes can only be obtained at a limited number of stations and only on rainy days. The lack of continuous information makes it limited to analyze the effects of water vapor propagation and alternating monsoon and westerlies. In addition, the seasonal pattern and the spatial variation of water isotopes can strongly influenced by synoptic-scale processes, through their influence on moisture source, transport, convection and mixing processes (Klein et al., 2015;Sánchez-Murillo et al., 2019;Wang et al., 2021), which requires higher frequency observations. For example, some studies founded the impact of tropical cyclones (Gedzelman, 2003;Bhattacharya et al., 2022) the Northern Summer Intra-Seasonal Oscillation (BSISO) (Kikuchi, 2021), local or large-scale convections (Shi et al., 2020), cold front passages (Aemisegger et al., 2015), depressions(Saranya et al., 2018), and anticyclones (Khaykin et al., 2022) on water isotopes in the Asian region. Additional data and analysis refining our understanding of controls on the spatial and temporal variation of water isotopes in low-latitude regions therefore are needed.

Unlike precipitation, water vapor enters all stages of the hydrological cycle, experiencing frequent and intensive exchange with other water phases, in particular, directly linked with

water isotope fractionation. Furthermore, vapor isotopes can be measured in regions and periods without precipitation, and therefore, have significant potential to trace how water is transported, mixed, and exchanged (Galewsky et al., 2016;Noone, 2008), and to diagnose large-scale water cycle dynamics. Water vapor isotope data have been applied to various applications ranging from the marine boundary layer to continental recycling, and to various geographical regions from tropical convection to polar climate reconstructions (Galewsky et al., 2016). The development of laser-based spectroscopic isotope analysis made the precise, high-resolution and real-time measurements of both vapor $\delta^{18}O$ and $\delta^{2}H$ available in recent decades. However, most of the in-situ observation of water vapor isotopes are also station-based (e.g., (Li et al., 2020;Tian et al., 2020;Steen-Larsen et al., 2017;Aemisegger et al., 2014)), or performed during ocean cruises (Thurnherr et al., 2020;Bonne et al., 2019;JingfengLiu et al., 2014;Kurita, 2011;Benetti et al., 2017). One study made vehicle-based in-situ observations to document spatial variations, but this was restricted to the Hawaii island (Bailey et al., 2013). These observations provided new insight on moisture sources, synoptic influences, and sea surface evaporation fractionation processes. However, in-situ observations documenting continuous spatial variations at the continental scale do not exist. This paper presents the first isotope dataset documenting the spatial variations of vapor isotopes over a large continental region (over 10000 km) both during the pre-monsoon and monsoon periods, based on vehicle-based in-situ observations..

After describing our observed time series along the route (section 3.1 and 3.2), we quantify the relative contributions of seasonal-mean spatial variations and synoptic-scale variations that locally disturb the seasonal-mean to our observed time series (section 3.3). We show that our observed variations in both seasons are dominated by spatial variations, but are influenced by significant synoptic-scale variations during the monsoon period. On the basis of this, we then focus on analysing the main mechanisms underlying these distributions (section 4). Collectively, these data and analyses provide refined understanding of how the interaction of the summer monsoon and westerly circulation control water isotope ratios in East Asia.

2. Data and methods

2.1 Geophysical description

We conducted two campaigns to monitor vapor isotopes across a large part of China during the pre-monsoon (3rd to 26th March, 2019) and the monsoon (28th July to 18th August, 2018) periods, using a newly designed vehicle-based vapor isotope monitoring system (Fig.S1). The two campaigns run along almost the same route, with slight deviation in the far northeast of China (Fig.1). Our vehicle started from Kunming city in southwestern China, traveled northeast to Harbin, then turned to northwestern China (Hami), and returned to Kunming. The expedition traversed most of eastern China, with a total distance of above 10000km for each campaign.

130
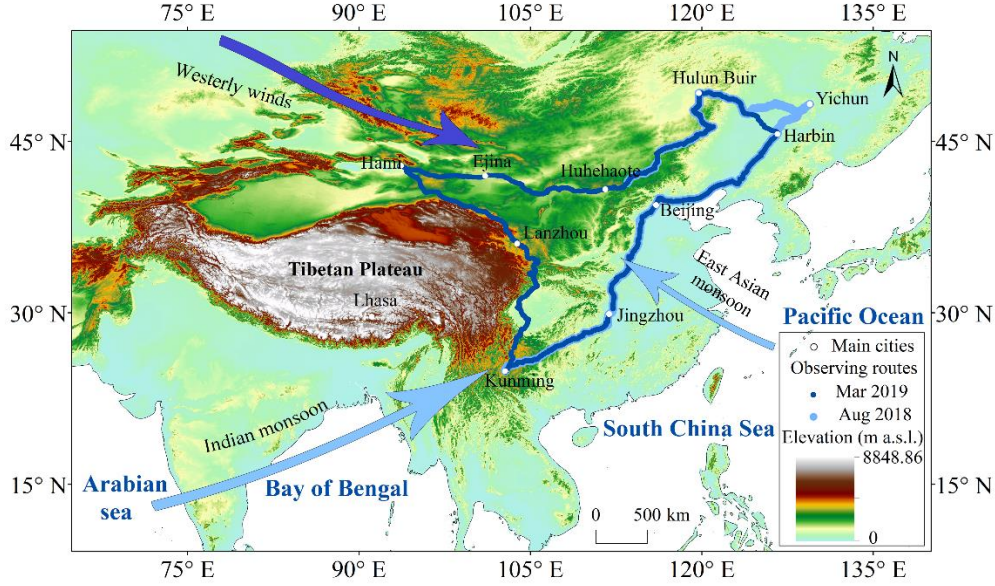
Fig.1. Topographical map of China, showing survey routes and the main atmospheric circulation systems (arrows). Dark blue dots indicate the observation route for the 2019 pre-monsoon period, and light blue dots show the observation route for the 2018 monsoon period, with a slight deviation in the northeast.

2.2 Vapor isotope measurements

2.2.1 Isotopic definitions.

Isotopic compositions of samples were reported as the relative deviations from the standard water (Vienna Standard Mean Ocean Water, VSMOW), using the δ-notion (McKinney et al., 1950), where R_{sample} and R_{VSMOW} are the isotopic ratios ($H_2^{18}O/H_2^{16}O$ for $\delta^{18}O$, and $^1H^2H^{16}O/H_2^{16}O$ for δ^2H) of the sample and of the VSMOW, respectively:

$$\delta = (R_{sample}/R_{VSMOW}-1)*1000 \tag{1}$$

The second-order d-excess parameter is computed based on the commonly used definition (Dansgaard, 1964). The d-excess is usually interpreted as reflecting the moisture source and evaporation conditions *(Jouzel et al., 1997)*, since the d-excess is more sensitive to non-equilibrium fractionation occurs than $\delta^{18}O$:

$$d\text{-excess} = \delta^2H-8*\delta^{18}O \tag{2}$$

2.2.2 Instrument

We used a Picarro 2130i CRDS water vapor isotope analyzer fixed on a vehicle to obtain large-scale in-suit measurements of near-surface vapor isotopes along the route. The analyzer was powered by a lithium battery on the vehicle, enabling over 8 hours operation with a full charge. Therefore, we only made measurements in daytime and recharged the battery at night. The ambient air inlet of the instrument was connected to the outside of the vehicle, which was 1.5 m above ground, with a waterproof cover to keep large liquid droplets from entering. A portable GPS unit was used to record position data along the route. The measured water vapor mixing ratio and the $\delta^{18}O$ and δ^2H were obtained with a temporal resolution of ~1 second. The dataset present in this study had been averaged to a 10-min temporal resolution after calibration, with the horizontal footprint of about 15 km.

159   A standard delivery module (SDM) was used for the vapor isotope calibration during the
160   surveys. The calibration protocols consists of humidity calibration (section 2.2.3), standard
161   water calibration (section 2.2.4), and error estimation (section 2.2.5), following the methods of
162   (Steen-Larsen et al., 2013).
163
164   2.2.3 Humidity-dependent isotope bias correction
165   The measured vapor isotopes are sensitive to air humidity (JingfengLiu et al.,
166   2014;Galewsky et al., 2016), which vary substantially across our sampling route. The specific
167   humidity measured by Picarro is very close to that measured by an independent sensor installed
168   in the vehicle (Fig.4). The correlation between the humidity measured by the Picarro and the
169   independent sensor are over 0.99, the slopes are approximately 1 and the average deviation are
170   less than 1 g/kg both during pre-monsoon and monsoon periods. We develop a humidity-
171   dependent isotope bias correction by measuring a water standard at different water
172   concentration settings using the SDM. We define a reference level of 20,000 ppm of vapor
173   humidity for our analysis (Eq. 3), since water vapor isotope measurement by Picarro is
174   generally most accurate at this humidity, the calibrated vapor isotope with different air humidity
175   would be (JingfengLiu et al., 2014;Schmidt et al., 2010):

176    $\delta_{measured} - \delta_{humidity\ calibration} = f\ (humidity_{measured} - 20000)$ (3)

177   where $\delta_{measured}$ represents the measured vapor isotopes (the raw data), $\delta_{humidity\ calibration}$
178   denotes the calibrated vapor isotopes, f is the equation of δ as a function of humidity , and
179   humidity is in ppm. E.g., if we measured that f is $\delta = a*\ln\ (humidity)+b$ by measuring standard
180   water with different humidity, then the full equation for humidity-dependent isotope bias
181   correction would be $\delta_{measured} - \delta_{humidity\ calibration} = a*\ln\ (humidity_{measured})+b - (a*\ln\ (20000)+b)$.
182   We performed the humidity calibration before and after each campaign. In the calibration,
183   the setting of humidity covered the actual range of humidity in the field. In the dry pre-monsoon
184   period of 2019, the humidity was less than 5000 ppm along a large part of the route. In this case,
185   we performed additional calibration tests with the humidity less than 5000 ppm after the field
186   observations to guarantee the accuracy of the calibration results. The humidity-dependence
187   calibration function is considered constant throughout each campaign (which each lasted less
188   than 24 days).
189
190   2.2.4 Measurement normalization
191   All measured vapor isotope values were calibrated to the VSMOW-SLAP scale using two
192   laboratory standard waters ($\delta^{18}O = -10.33‰$ and $\delta^2H = -76.95‰$, $\delta^{18}O = -29.86‰$ and $\delta^2H =$
193    $-222.84‰$) covering the range of the expected ambient vapor values. We made the
194   normalization test prior to the daily measurements (two humidity levels for each standard
195   water). We adjusted the amount of the liquid standard injected everyday to keep the humidity
196   of the standard waters consistent with the outside vapor measurements. Our calibration shows
197   that no significant drift of the standard values were observed over time in the observation
198   periods (For two standard waters, the standard deviation of standard measurements are 0.2‰
199   and 0.11‰ for $\delta^{18}O$, and 1.16‰ and 1.2‰ for δ^2H during the pre-monsoon period of 2019.
200   During the monsoon period of 2018, the standard deviation of standard measurements are 0.09‰
201   and 0.06‰ for $\delta^{18}O$, and 0.6‰ and 0.33‰ for δ^2H.).
202

203   2.2.5 Error estimation

204   We estimate the uncertainty based on the error between the measured (after calibration)
205   and true values of the two standards used during the campaigns. The estimated uncertainty is
206   in the range of -0.05~0.17 for $\delta^{18}O$, 0.11~1.19 for δ^2H, and -0.81~1.23‰ for d-excess during
207   the pre-monsoon period of 2019, with the humidity ranges from 2000 ppm to 29000 ppm.
208   During the monsoon period of 2018, the range of uncertainty is -0.10~0.55‰ for $\delta^{18}O$, -
209   0.94~3.74‰ for δ^2H, and -1.18~1.49‰ for d-excess, with the humidity ranges from 4000 to
210   34000 ppm.

211

212   2.2.6 Data processing

213   A few isotope measurements with missing GPS information were excluded from the
214   analysis. Since we want to focus on large-scale variations, we also removed the observations
215   during raining or snowing, to avoid situations where hydrometeor evaporation significantly
216   influenced the observations (Tian et al., 2020). Such data represents only 0.03% and 0.05% of
217   our observations, respectively (totally 48 data during pre-monsoon season and 59 data during
218   the monsoon season). We observed several d-excess pulses with extremely low values as low
219   as −18.0‰ during the pre-monsoon period and -4.9‰ during the monsoon period. These low
220   values are unusual in previous natural vapor isotope studies and occurred mostly when the
221   measurement vehicle was entering or leaving cities and/or stuck in traffic jams, and have a
222   much lower intercept in the linear $\delta^{18}O$ - δ^2H relationship (Fig.S6). Previous studies on urban
223   vapor isotopes (Gorski et al., 2015;Fiorella et al., 2018;Fiorella et al., 2019) showed that the
224   vapor d-excess closely tracked changes in CO_2 through inversion events and during the daily
225   cycle dominated by patterns of human activity, and combustion-derived water vapor is
226   characterized by a low d-excess value due to its unique source. We also find that the d-excess
227   values are especially low when the vehicle was in cities in the afternoon. The values increased
228   to normal during the night. This diurnal cycle is likely related to the emission intensity and
229   atmospheric processes (Fiorella et al., 2018). Some of these d-excess anomalies are not
230   excluded from being affected by the baseline effects emerging from rapid changes in
231   concentrations of different trace gases (Johnson and Rella, 2017;Gralher et al., 2016). We
232   therefore excluded these data (133 data points during the pre-monsoon period and 62 data points
233   during the monsoon period, represents 0.10% and 0.06% of our observations, respectively) in
234   the discussion on the general spatial feature (except Fig.4). Outside towns, country sources,
235   such as irrigation, farms, and power plants, cannot be completely ruled out. However, we expect
236   their influence to be much smaller than large-scale spatial variations.

237   2.3 Meteorological observations

238   We fixed a portable weather station on the roof of the vehicle to obtain air temperature (T),
239   dew-point temperature (T_d), air pressure (Pres) and relative humidity (RH). All sensors were
240   located near the ambient air intake. The specific humidity (q) of the near-surface air was
241   calculated from T_d and Pres. Meteorological data, GPS location data and vapor isotope data
242   were synchronized according to their measurement times. And all of them also had been
243   averaged to a 10-min temporal resolution.

244   National Centers for Environmental Prediction/ National Center for Atmospheric Research
245   (NCEP/NCAR) 2.5-deg global reanalysis data are used to determine the large-scale factors

246 influencing the spatial pattern of the vapor isotopes, including the surface T, q, U-wind and V-
247 wind, and RH, which are available at
248 https://psl.noaa.gov/data/gridded/data.ncep.reanalysis.surface.html. Some missing
249 meteorological data (during the pre-monsoon period: q on 8th March and 18th March 2019;
250 during the monsoon period: T and q from 28th July to 31st July, q on 5th August) along the survey
251 routes due to instrument failure are acquired from the NCEP/NCAR reanalysis data. To match
252 the vapor isotope data along the route, we linearly interpolate the NCEP/NCAR data to the
253 location and time of each measurement. The interpolated T and q from NCEP/NCAR are highly
254 correlated with our measurement as shown in Figure 4h and j. The 1-deg precipitation amount
255 (P) from the Global Precipitation Climatology Project (GPCP) are used
256 (https://www.ncei.noaa.gov/data/global-precipitation-climatology-project-gpcp-daily/access/).
257 When comparing the time series of GPCP data with our observed isotopes, we linearly
258 interpolate the daily GPCP data to the location of each observation location (P-daily).We also
259 used the average of the GPCP precipitation over the entire observation period of about one
260 month for each observation location (P-mean). The 2.5-deg outgoing longwave radiation (OLR)
261 data can be obtained from NOAA
262 (http://www.esrl.noaa.gov/psd/data/gridded/data.interp_OLR.html).

263 2.4 Back-trajectory calculation and categorizing regions based on air mass origin

264   The vapor isotope composition is a combined result of moisture source (Tian et al.,
265 2007;Araguás-Araguás et al., 1998), condensation and mixing processes along the moisture
266 transport route (Galewsky et al., 2016). To interpret the observed spatial-temporal distribution
267 of vapor isotopes, we start with a diagnosis of the geographical origin of the air masses and
268 then analyze the processes along the back-trajectories.
269   To trace the geographical origin of the air masses, the HYSPLIT-compatible
270 meteorological dataset of the Global Data Assimilation System (GDAS) is used (available at
271 ftp://arlftp.arlhq.noaa.gov/pub/archives/gdas1/). We select the driving locations every 2 hours
272 as starting points for the backward trajectories, and make 10-day back-trajectories from 1000
273 m above ground using the Hybrid Single Particle Lagrangian Integrated Trajectory Model 4
274 (HYSPLIT4) (Draxler and Hess, 1998). This is representative of the water vapor near the
275 ground (Guo et al., 2017;Bershaw et al., 2012), since most water vapor in the atmosphere is
276 within 0–2 km above ground level (Wallace and Hobbs, 2006). The T, q, P and RH along the
277 back-trajectories are also interpolated by HYSPLIT4 model (Fig.2).
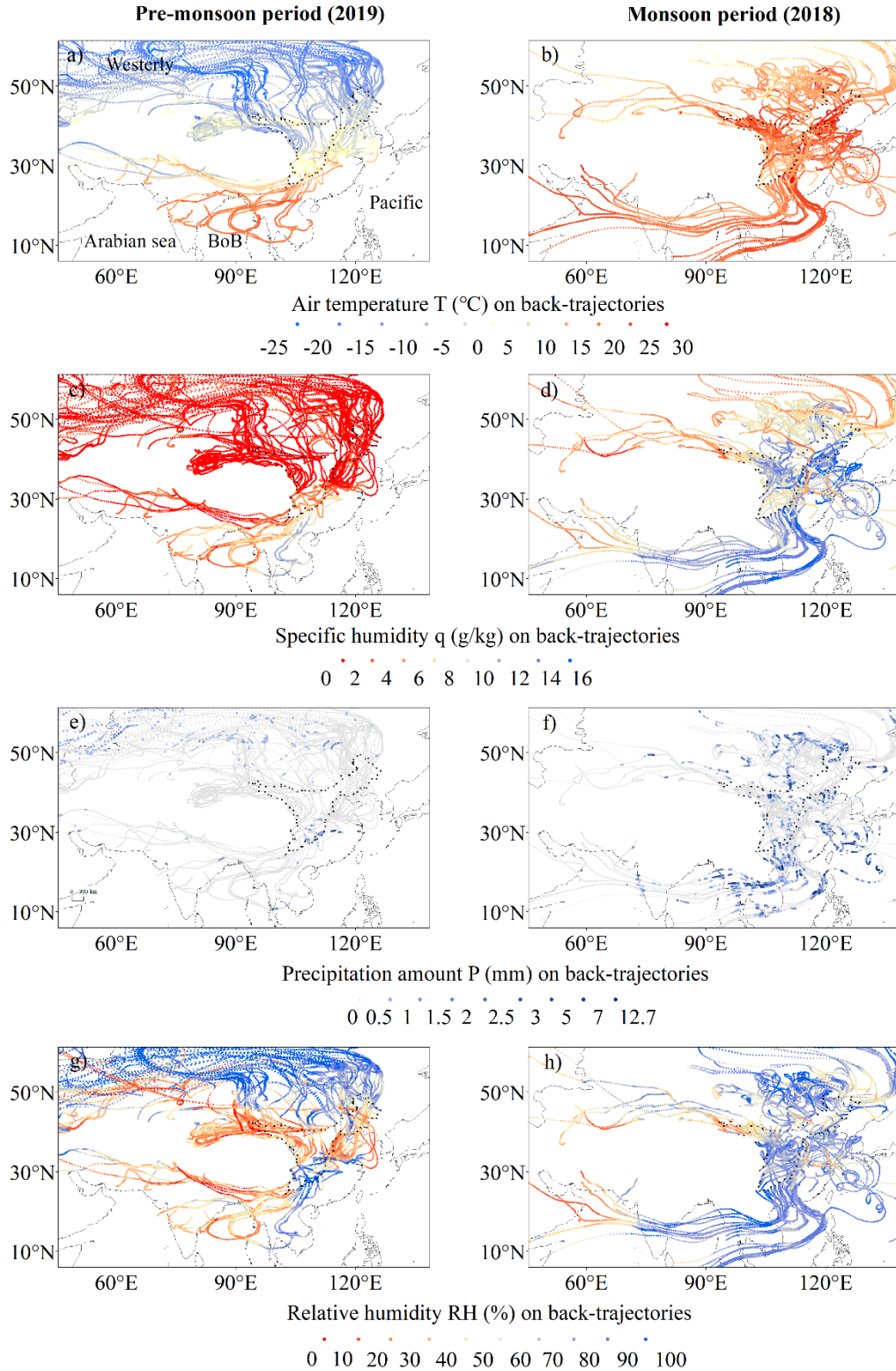
Fig.2 Meteorological conditions simulated by HYSPLIT4 model along the 10-day air back-trajectories for the on-route sampling positions during the two surveys: (a, b) air temperature T (°C), (c, d) specific humidity q (g/kg), (e, f) precipitation amount P (mm) and (g, h) relative humidity RH (%). The left panel is for the pre-monsoon period and the right is for the monsoon period. The driving locations and time every 2 hours are used as starting points. Note: BoB is the abbreviation for the Bay of Bengal.
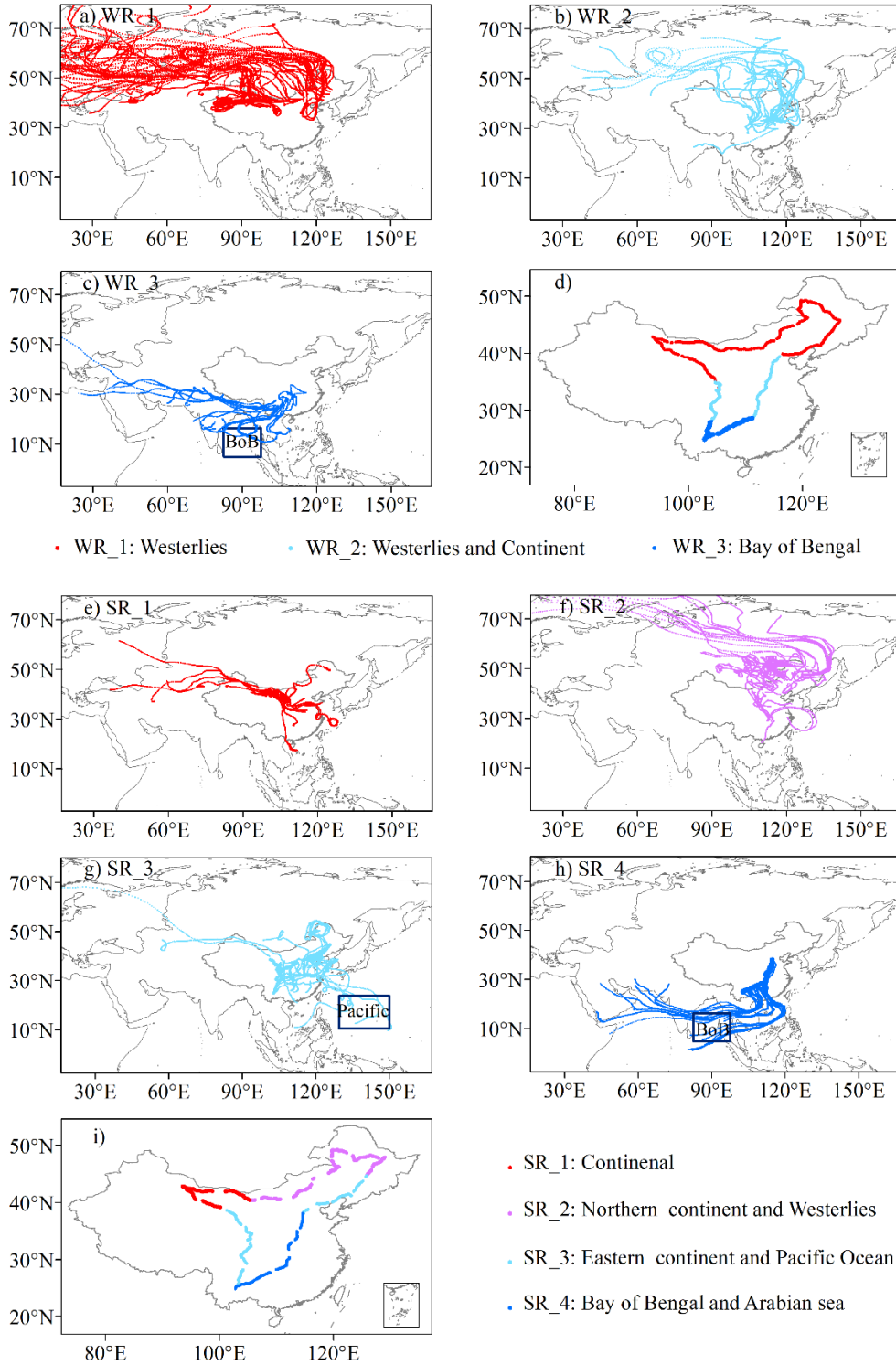
Fig.3 The backward trajectory results (a, b and c for the pre-monsoon period, and e, f, g and h for the monsoon period) and the dividing of the study zones based on geographical origin of the air masses (d for the pre-monsoon period and i for the monsoon period). Note: BoB is the abbreviation for the Bay of Bengal.

Based on the tracing results from HYSPLIT4 model, we speculate on the potential water vapor sources (Fig.3 and Table 1):

During the pre-monsoon period, we categorize our domain into 3 regions (Table 1).

293   (1) In northern China (WR_1), the air is mainly advected by the Westerlies.

294   (2) In central China (WR_2), the air also comes from the Westerlies but with a slower wind
295 speed (as shown by the shorter trajectories in 10 days), suggesting potential for greater
296 interaction with the land surface and more continental recycling as moisture source.

297   (3) In southern China (WR_3), trajectories come from the Southwest and South with
298 marine moisture sources from the Bay of Bengal (BoB).

299   During the monsoon period, we categorize our domain into 4 regions (Table 1):

300   (1) In northwestern China (SR_1), most air masses also spend considerable time over the
301 continent, suggesting some of the vapor can be recycled by continental recycling.

302   (2) In northeastern China (SR_2), trajectories mainly come from the North and though the
303 Westerlies.

304   (3) In central China (SR_3), both in its eastern (from Beijing to Harbin) and western part,
305 trajectories mainly come from the East. This suggests that vapor mainly comes from the Pacific
306 Ocean, or from continental recycling over eastern and central China.

307   (4) In southeastern China (SR_4), trajectories come from the South, suggesting marine
308 moisture sources from the Arabian Sea and the BoB.

309

310   Table 1. The dividing of the study zones based on moisture sources and corresponding
311   vapor $\delta^{18}O$-δ^2H relationship

Pre-monsoon period (2019)				
	Water sources (Fig.3)	Region (China)	Climate background	$\delta^{18}O$-δ^2H relationship
WR_1	Westerlies	The north	Westerlies domain	$\delta^{18}O=8.04\delta^2H+12.00$ (r^2=0.99, n=750, q<0.01)
WR_2	Westerlies and Continent	The middle	Transition domain	$\delta^{18}O=8.26\delta^2H+23.15$ (r^2=0.99, n=281, q<0.01)
WR_3	Bay of Bengal (BoB)	The south	Monsoon domain	$\delta^{18}O=7.98\delta^2H+17.13$ (r^2=0.94, n=158, q<0.01)
Monsoon period (2018)				
	Water sources (Fig.3)	Region (China)	Climate background	$\delta^{18}O$-δ^2H relationship
SR_1	Continent	The northwest	Transition domain	$\delta^{18}O=8.31\delta^2H+20.92$ (r^2=0.99, n=200, q<0.01)
SR_2	Northern continent & Westerlies	The northeast	Transition domain	$\delta^{18}O=7.53\delta^2H+5.13$ (r^2=0.98, n=294, q<0.01)
SR_3	Eastern continent & Pacific Ocean	The middle and west	Transition domain	$\delta^{18}O=7.49\delta^2H+7.09$ (r^2=0.97, n=271, q<0.01)
SR_4	BoB & Arabian sea	The southeast	Monsoon domain	$\delta^{18}O=8.21\delta^2H+17.81$ (r^2=0.99, n=195, q<0.01)

312

313   2.5 General circulation model simulation and satellite measurements

314   To disentangle the spatial and synoptic influences, we use surface layer variables from an
315 isotope-enabled general circulation model (Iso-GSM) simulations (Yoshimura and Kanamitsu,
316 2009) at 1.915° x 1.875° and the lowest level (the altitude are about 2950m) isotope retrievals

from satellite Infrared Atmospheric Sounding Interferometer (IASI) at 1°x1°. For both dataset, we use the outputs corresponding to the observation location and the observation date (daily outputs), and the multi-year monthly-mean outputs (March monthly for the pre-monsoon period and August monthly for the monsoon period) for each observation location from 2015 to 2020. When interpolating daily/multi-year monthly outputs, we select the nearest grid point for a given latitude and longitude of each measurement. For Iso-GSM simulations, because of the coarse resolution of the model, there is a difference between the altitude observed along the sampling route and that of the nearest grid point. Therefore, we correct the outputs of Iso-GSM for this altitude difference (the method is given in III. Supplementary Text). Since the satellite only retrieves δ^2H, we just use δ^2H outputs of Iso-GSM and satellite to quantify the relative contributions of seasonal-mean and synoptic-scale variations (section 3.3). Other than that, our discussion focuses on $\delta^{18}O$ and d-excess. The variations of δ^2H are consistent with those of $\delta^{18}O$. We also interpret the biases in Iso-GSM after we understand the factors influencing the spatial and seasonal variation of vapor isotopes (section 4.6).

2.6 Method to decompose the observed daily variations

The temporal variations observed along the route for a given period represent a mixture of synoptic-scale perturbations, and of seasonal-mean spatial distribution:

$$\delta^2H_{\_daily}= \delta^2H_{\_seaso} + \delta^2H_{\_synoptic} \qquad (4)$$

The first term represents the contribution of seasonal-mean spatial variations, whereas the second term represents the contribution of synoptic-scale variations. Since these relative contributions are unknown, we use outputs from Iso-GSM and IASI. The daily variations of δ^2H simulated by Iso-GSM also represent a mixture of synoptic-scale perturbations and seasonal-mean spatial distribution, but with some errors relative to reality:

$$\delta^2H_{daily\_Iso\text{-}GSM} = \delta^2H_{\_seaso\_Iso\text{-}GSM} + \delta^2H_{\_synoptic\_Iso\text{-}GSM} \qquad (5)$$

where $\delta^2H_{daily\_Iso\text{-}GSM}$ is the daily outputs of δ^2H for each location, $\delta^2H_{\_seaso\_Iso\text{-}GSM}$ is the multi-year monthly outputs of δ^2H for each location, and $\delta^2H_{\_synoptic\_Iso\text{-}GSM} = \delta^2H_{\_daily\_Iso\text{-}GSM} - \delta^2H_{\_seaso\_Iso\text{-}GSM}$, each of these terms are affected by errors relative to observations:

$$\delta^2H_{daily\_Iso\text{-}GSM} = \delta^2H_{\_daily} + \in = (\delta^2H_{\_seaso} + \in_{\_seaso}) + (\delta^2H_{\_synoptic} + \in_{\_synoptic}) \qquad (6)$$

where $\in_{\_seaso}$ and $\in_{\_synoptic}$ are the errors on $\delta^2H_{\_seao\_Iso\text{-}GSM}$ and $\delta^2H_{\_synoptic\_Iso\text{-}GSM}$ relative to reality, respectively, $\in$ is the sum of $\in_{\_seaso}$ and $\in_{\_synoptic}$.

Correspondingly, $\delta^2H_{\_daily} = \delta^2H_{\_daily\_Iso\text{-}GSM} - \in = (\delta^2H_{\_seaso\_Iso\text{-}GSM} - \in_{\_seaso}) + (\delta^2H_{\_synoptic\_Iso\text{-}GSM} - \in_{\_synoptic}) \qquad (7)$

These individual error components $\in_{\_seaso}$ and $\in_{\_synoptic}$ are unknown, but we know the sum of them ($\in$), i.e. the difference between daily outputs and observations. For the decomposition, we made two extreme assumptions to estimate upper and lower bounds on the contribution values:

(1) If we assume that the error is purely synoptic, i.e. $\in = \in_{\_synoptic}$, and $\in_{\_seaso} =0$, then:

$$\delta^2H_{\_daily} = \delta^2H_{\_seaso\_Iso\text{-}GSM} + (\delta^2H_{\_synoptic\_Iso\text{-}GSM} - \in) \qquad (8)$$

To evaluate the contribution of these two terms, we calculate the slopes of $\delta^2H_{\_daily}$ as a function of $\delta^2H_{\_seaso\_Iso\text{-}GSM}$ ($a_{\_seaso}$), and of $\delta^2H_{\_daily} - \delta^2H_{\_seaso\_Iso\text{-}GSM}$ ($a_{\_synoptic}$). The relative contributions of spatial and synoptic variations correspond to $a_{\_seaso}$ and $a_{\_synoptic}$ respectively. This will be the upper bound for the contribution of synoptic-scale variations, since some of

360   the systematic errors of Iso-GSM will be included in the synoptic component. This is equivalent

361   to using the seasonal-mean of Iso-GSM and the raw time series of observations.

362   (2) If we assume that the error is purely seasonal-mean, i.e. $\in = \in_{\_seaso}$, and $\in_{\_synoptic} = 0$,

363   then:

364        $\delta^2 H_{\_daily} = (\delta^2 H_{\_seaso\_Iso\text{-}GSM} - \in) + \delta^2 H_{\_synoptic\_Iso\text{-}GSM}.$ (9)

365   To evaluate the contribution of these two terms, we calculate the slopes of $\delta^2 H_{\_daily\_Iso\text{-}GSM}$

366   as a function of $\delta^2 H_{\_seaso\_Iso\text{-}GSM} - \in$ ($a_{\_seaso}$), and of $\delta^2 H_{\_daily} - (\delta^2 H_{\_seaso\_Iso\text{-}GSM} - \in)$ ($a_{\_synoptic}$).

367   This will be the lower bound for the contribution of synoptic-scale variations, since we expect

368   Iso-GSM to underestimate the synoptic variations.

369   The same analysis is also performed for $\delta^2 H$ retrieved from IASI, and the Iso-GSM

370   simulation q (Table 2) and reanalysis q (Table 3).

371   3. Spatial and seasonal variations

372   3.1 Raw time series

373   Our survey of the vapor isotopes yields two snapshots of the isotopic distribution along

374   the route (Fig.4 & Fig.5). Figure 4 shows the variations of observed 10-min averaged surface

375   vapor $\delta^{18}O$ and d-excess along the survey route across China during the pre-monsoon and

376   monsoon campaigns. The figure also shows the concurrent meteorological data from the

377   weather station installed on the vehicle and the water vapor content recorded by the Picarro

378   water vapor isotope analyzer as a comparison. We extract daily precipitation amount (P-daily)

379   and average precipitation amount over the entire observation period of about one month for

380   each observation location (P-mean) (mm/day) from GPCP. The vapor $\delta^{18}O$ shows high

381   magnitude variations in both seasons. A general decreasing-increasing trend overlapped with

382   short-term fluctuations is observed during the pre-monsoon period, whereas no general trend

383   but frequent fluctuations characterized the monsoon period. The $\delta^{18}O$ range is much larger

384   during the pre-monsoon period (varying between -44‰ and -8‰) than during the monsoon

385   period (from -11‰ to -23‰). Most measured vapor d-excess values ranges from 5 to 25‰

386   during the pre-monsoon period and from 10 to 22‰ during the monsoon period.

387   Comparison with the concurrently observed meteorological data shows a robust air

388   temperature (T) dependence of the vapor $\delta^{18}O$ variations. In particular, the general trend of $\delta^{18}O$

389   is roughly consistent with T variation during the pre-monsoon period (Fig.4a and g). During

390   the pre-monsoon period, humidity (Fig.4e and i), P-mean (Fig.4k) and vapor $\delta^{18}O$ (Fig.4a) are

391   much higher in southwestern China (at the beginning and end of the campaign) than in any

392   other regions. Humidity, q, and P-mean also vary consistently throughout the route during the

393   monsoon period (Fig.4f, j, l). Synoptic effects on the observed vapor isotopes are discussed in

394   detail in Section 4.3 and 4.6.
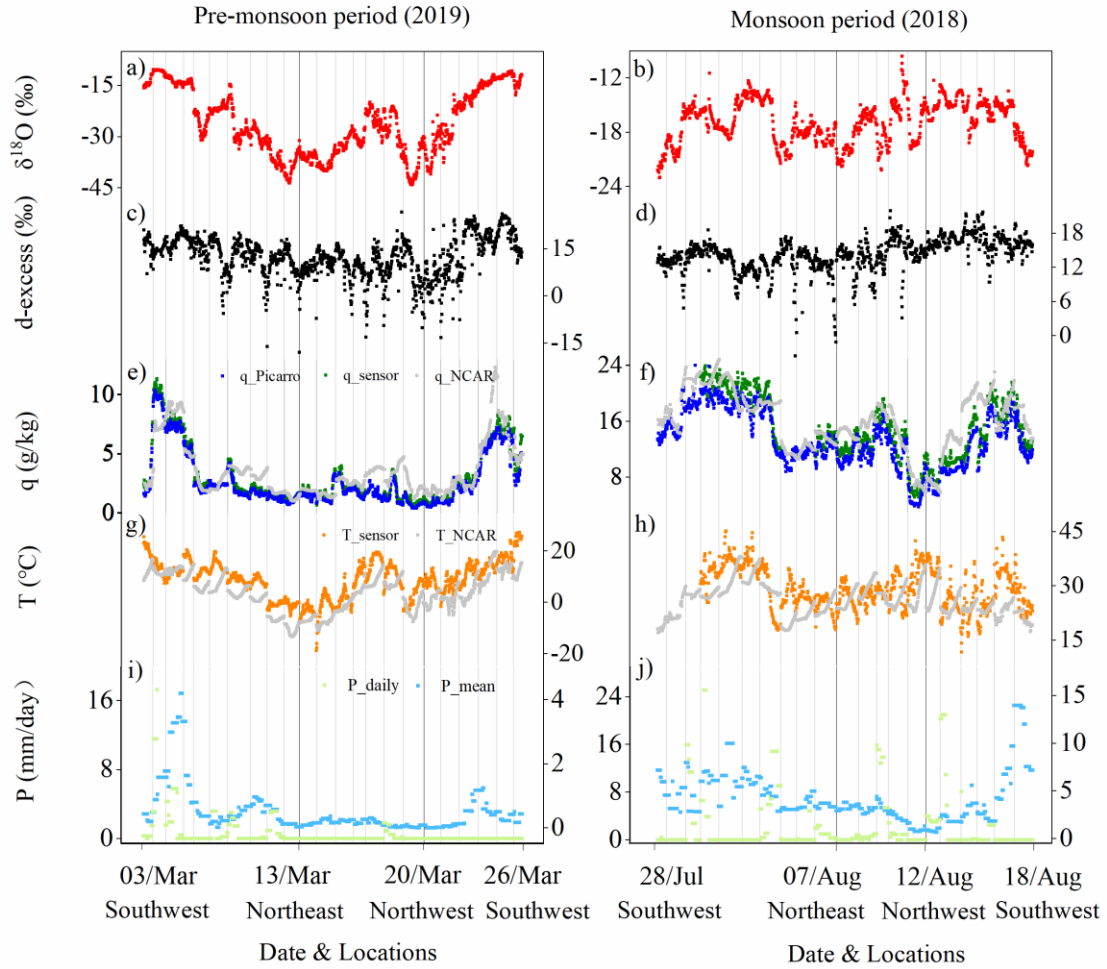
Fig.4. Measured vapor isotopic compositions and concurrent meteorological conditions along the survey routes during the pre-monsoon period (the left panel) and monsoon period (the right panel). (a, b) vapor $\delta^{18}O$ (‰); (c, d) vapor d-excess (‰); (e, f) specific humidity q (g/kg) measured by sensor (in green), measured by Picarro (in blue) and linearly interpolate from NCAR reanalysis (in grey); (g, h) air temperature T (℃) measured by Picarro (in orange) and linearly interpolate from NCAR reanalysis (in grey); (i, j) the daily precipitation amount P-daily (in green, mm/day) and average precipitation amount over the entire observation period of about one month for each observation location P-mean (in blue, mm/day) extract from GPCP. Notes: the gray dots are T and q linearly interpolate from NCAR reanalysis to compensate for missing observations; Gray vertical lines space the observations for one day.

3.2 Spatial variations

The spatial distribution of the observed vapor $\delta^{18}O$ and d-excess during the two surveys in different seasons are presented in Figure 5. During the pre-monsoon period, we find a south-north gradient of vapor $\delta^{18}O$ (Fig.5a). The vapor $\delta^{18}O$ ranges from -8~ -16‰ in southern China to as low as -24 ~ -44‰ in the North. A roughly similar spatial pattern is observed for the vapor d-excess during the pre-monsoon period (Fig.5c). The d-excess value ranges from 10 to 30‰ in southern China and from -10 to +20‰ (most observations with values from 5 to +20‰) in northern China. In previous studies, a higher precipitation d-excess during the pre-monsoon period was also observed in the Asian monsoon region owing to the lower relative humidity

(RH) at the surface in the moisture source region (Tian et al., 2007;Jouzel et al., 1997). The same reason probably explains the higher vapor d-excess in southern China observed here. Alternatively, the high d-excess in south China could also result from the moisture flow from Indian/Pacific Ocean, or from the deeper convective mixed layer in south China compared to north China. The lower d-excess values (as low as −10‰ to 10‰) in northern China (between 38°N and 51°N) have rarely been reported in earlier studies. The spatial distribution of the observed vapor d-excess could reflect the general latitudinal gradient of d-excess observed at the global-scale, with a strong poleward decrease in midlatitudes (between around 20 to 60°), which were found in previous studies on large-scale distribution of d-excess in vapor (Thurnherr et al., 2020;Benetti et al., 2017) and precipitation (Risi et al., 2013a;Terzer-Wassmuth et al., 2021;Pfahl and Sodemann, 2014;Bowen and Revenaugh, 2003), based on both observations and modelling. During the monsoon period, the lowest values of vapor $\delta^{18}O$ are found in southwestern and northeastern China, with a range of -23‰ to -19‰ (Fig.5b). Higher vapor $\delta^{18}O$ values up to -11‰ are founded in central China. The vapor d-excess values (Fig.5d) in western and northwestern China (91°E-109°E, 24°N-43°N) are roughly between 16 and 22‰, higher than in eastern China (mostly between 0 and 16‰).
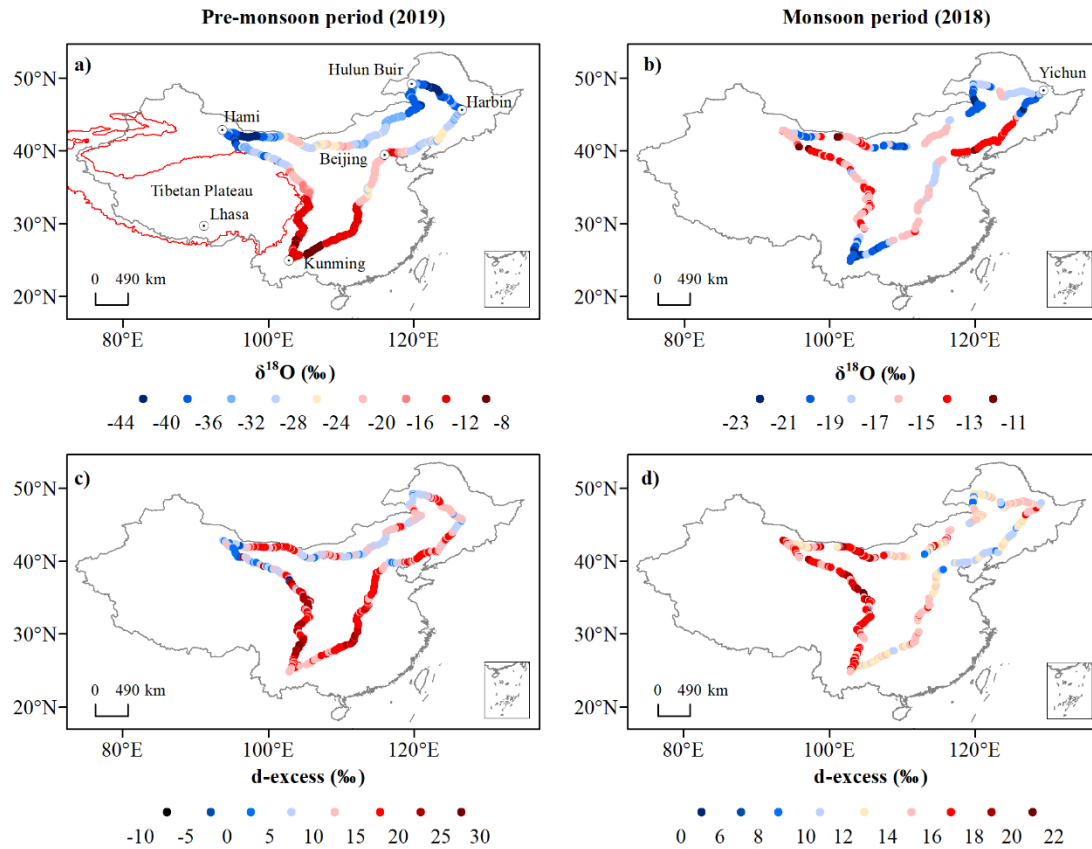
Fig.5. Spatial distribution of vapor $\delta^{18}O$ (a, b) and d-excess (c, d) during the pre-monsoon period (the left panel) and monsoon period (the right panel).

We don't know whether these apparent spatial variations represent the seasonal-mean, or whether it is mainly affected by synoptic perturbations. We therefore use Iso-GSM simulation results and IASI satellite measurements to quantify the relative contributions of seasonal-mean and synoptic perturbations in section 3.3.

439   3.3 Disentangling seasonal-mean and synoptic variations

440   Figure 6 shows the comparison of the measured vapor δ^2H, simulated δ^2H from Iso-GSM,
441   and the δ^2H retrieves from IASI. Iso-GSM captures the variations in observed vapor δ^2H well
442   during the pre-monsoon period, with correlation coefficient of r = 0.84 (p<0.01) (Table S3).
443   The daily simulation results during the monsoon period are roughly in the range of observations,
444   but detailed fluctuations are not well captured, with r = 0.24 (p>0.05) (Table S3). The largest
445   differences occur in the SR_1 zone. IASI captures variations better than Iso-GSM during the
446   monsoon period, with r = 0.42 (p>0.05). IASI observes over a broad range of altitudes above
447   the ground level, so we expect lower δ^2H in IASI relative to ground-surface observations, but
448   the variations of vapor isotopes are vertically coherent (Fig.6). The systematic differences
449   between IASI and ground-level observations do not impact the slope of the correlation, and
450   thus doesn't impact the contribution estimation.

451

452
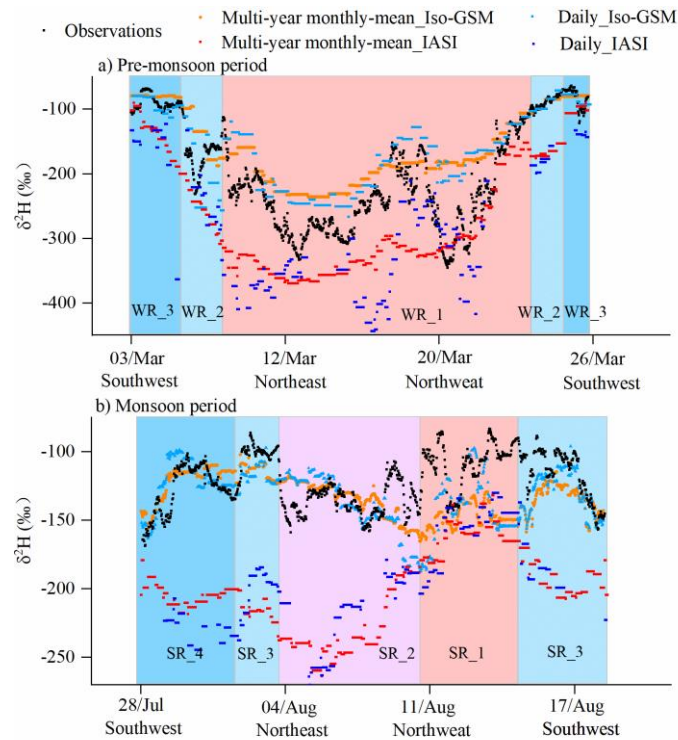
453   Fig.6 Comparison of observed vapor δ^2H (observations) with outputs of isotope-enabled
454   general circulation model Iso-GSM and satellite IASI during the pre-monsoon period (a) and
455   monsoon period (b). The results in this graph are from the daily and multi-year monthly
456   outputs for the sampling locations.

457   The multi-year monthly-mean of δ^2H are smoother but similar to those for the daily outputs
458   both from Iso-GSM and IASI (Fig.6). Using the method in section 2.6, taking into account the
459   error, we calculate the relative contribution ranges of the seasonal-mean and synoptic-scale on
460   our observed variations using q and δ^2H from Iso-GSM simulations, q from NCEP/NCAR
461   reanalysis, and δ^2H from IASI.

462   **Table 2** The relative contribution (in fraction) of spatial variations for a given season
463   (a_seaso) and of synoptic-scale variations (a_synopic) to the daily variations of q and δ^2H simulated

464 by Iso-GSM. We checked that the sum of a_seaso and a_synoptic is always 1. The two values
465 indicate the lower and upper bounds as calculated from equations 8 and 9.

Period	Data	Variables	Controbutions	
			$a_{\_seaso}$	$a_{\_synoptic}$
Pre-monsoon (2019)	Iso_GSM	q	0.73~1.02	0.27~-0.02
		$\delta^2 H$	0.60 ~0.98	0.40~0.02
	IASI	$\delta^2 H$	1.06~0.94	-0.06~0.06
Monsoon (2018)	Iso_GSM	q	0.71~0.82	0.29~0.18
		$\delta^2 H$	0.09~0.87	0.91~0.13
	IASI	$\delta^2 H$	0.53~0.84	0.47~0.16

466 **Table 3** The same as Table 2, but for reanalysis q.

Period	Variables	Controbutions	
		$a_{\_seaso}$	$a_{\_synoptic}$
Pre-monsoon (2019)	q	0.77~0.92	0.23~0.08
Monsoon (2018)	q	0.69~0.95	0.31~0.05

467 During the pre-monsoon period, based on both the Iso-GSM simulation and NCEP/NCAR
468 reanalysis, we can find that the seasonal-mean contribution to the measured q is higher than the
469 synoptic-scale contribution: a_seaso is 73%~102% from Iso-GSM and 77%~92% from reanalysis,
470 whereas a_synoptic is 27% ~ -2% from Iso-GSM and 23% ~ 8% from reanalysis (Table 2 and
471 Table3). The relative contribution of seasonal-mean spatial variations to the total measured
472 variations in $\delta^2 H$ (60% ~ 98%) is also higher than that of synoptic-scale variations (40% ~2%).
473 This suggests that the observed variability in q and $\delta^2 H$ is mainly due to spatial variability, and
474 marginally due to synoptic-scale variability. During the monsoon, seasonal-mean spatial
475 variations are also the main contributions to the observed variations of q (a_seaso is 71% ~ 82%
476 from Iso-GSM and 69% ~ 95% from reanalysis, whereas a_synoptic is 18% ~ 29% from Iso-GSM
477 and 5% ~ 31% from reanalysis). Since Iso-GSM doesn't capture daily variations of $\delta^2 H$ very
478 well during the monsoon period, the relative contribution has a large threshold range (a_seaso is
479 9%~87%, a_synoptic is 91% ~ 13%) after accounting for the errors. Therefore, we can not
480 conclude the dominate contribution on $\delta^2 H$ from Iso-GSM outputs. IASI, which has a higher
481 correlation with observations, provides an more credible range of a_seaso about 53% ~ 84%, and
482 a_synoptic 16% ~ 47%. These suggests that during the monsoon period, the synoptic contribution
483 can be significant, but not dominate. Having understood the factors influencing the spatial and
484 seasonal variation of vapor isotopes in section 4, we will be able to better understand the reasons
485 for the inconsistent performance of Iso-GSM during the pre-monsoon and monsoon periods (in
486 section 4.6).

487 3.4 Seasonal variations

488 During the monsoon season, synoptic-scale and intra-seasonal variations contribute
489 significantly to the apparent spatial patterns. However, since these variations are not dominate,
490 and have a smaller amplitude than seasonal differences, the comparison of the two snapshots
491 do provide a representative picture of the climatological seasonal difference.
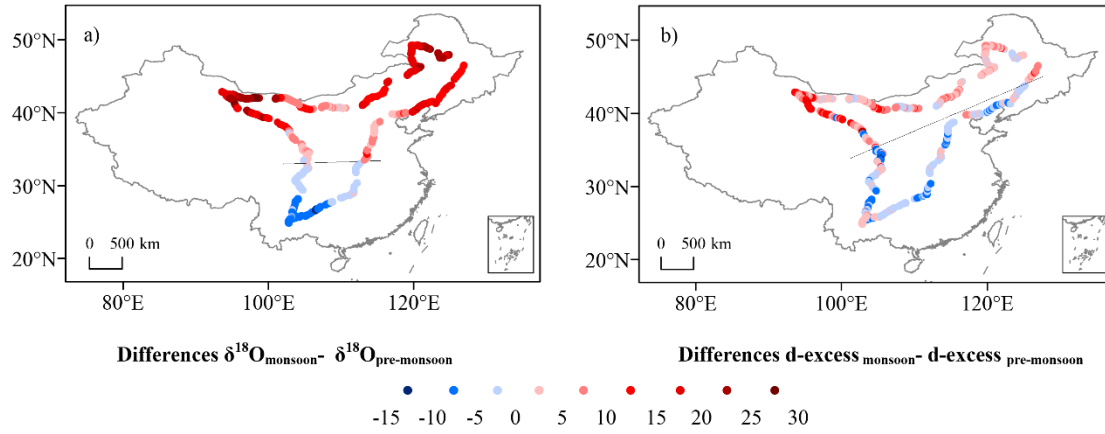
Fig.7 Spatial distribution of the isotope differences ($\delta^{18}O_{monsoon}$ - $\delta^{18}O_{pre-monsoon}$ (a) and d-excess$_{monsoon}$ - d-excess$_{pre-monsoon}$ (b)) for the observation locations. The solid black lines separate the areas of positive and negative values of the differences.

The climate in China features strong seasonality and it is captured in the snapshots of vapor isotopes (Fig.7). Since the observation routes of the two surveys are almost identical, we make a seasonal comparison of the observed vapor isotopes during the two surveys. The lines are drawn to distinguish between positive and negative values of seasonal isotopic differences. The seasonal differences $\delta^{18}O_{monsoon}$ - $\delta^{18}O_{pre-monsoon}$ (Fig.7a) show opposite sign in northern and southern China. In northern China, water vapor $\delta^{18}O$ values are higher during the monsoon period than during the pre-monsoon period, while the opposite are true in southern China. The boundary is located around 35 °N. The largest seasonal contrasts occur in southwest, northwest and northeast China, with seasonal $\delta^{18}O$ differences of -15 ‰, 30 ‰, and 30 ‰, respectively.

We also find a spatial pattern of vapor d-excess seasonality (Fig.7b). The line separating the areas of positive and negative values of the d-excess$_{monsoon}$ - d-excess$_{pre-monsoon}$ differences coincides with the 120 mm P-mean line (Fig.S2 f). In southeastern China, the water vapor d-excess is lower during the monsoon period than during the pre-monsoon period. The pattern of seasonal water vapor d-excess in northwestern China is the opposite. The two boundary lines separating the seasonal variations of $\delta^{18}O$ and d-excess do not overlap, suggesting different controls on water vapor $\delta^{18}O$ and d-excess.

4. Understanding the factors controlling the spatial and seasonal distributions

To interpret the spatial and seasonal variations observed both across China and in each region defined in section 2.4, we investigate q–δ diagrams (section 4.1), $\delta^{18}O$-δ^2H relationships (section 4.2), relationships with meteorological conditions at the local and regional scale (sections 4.3 and 4.4), the impact of air mass origin (section 4.5) and synoptic events (section 4.6).

520   4.1 q–δ diagrams

521
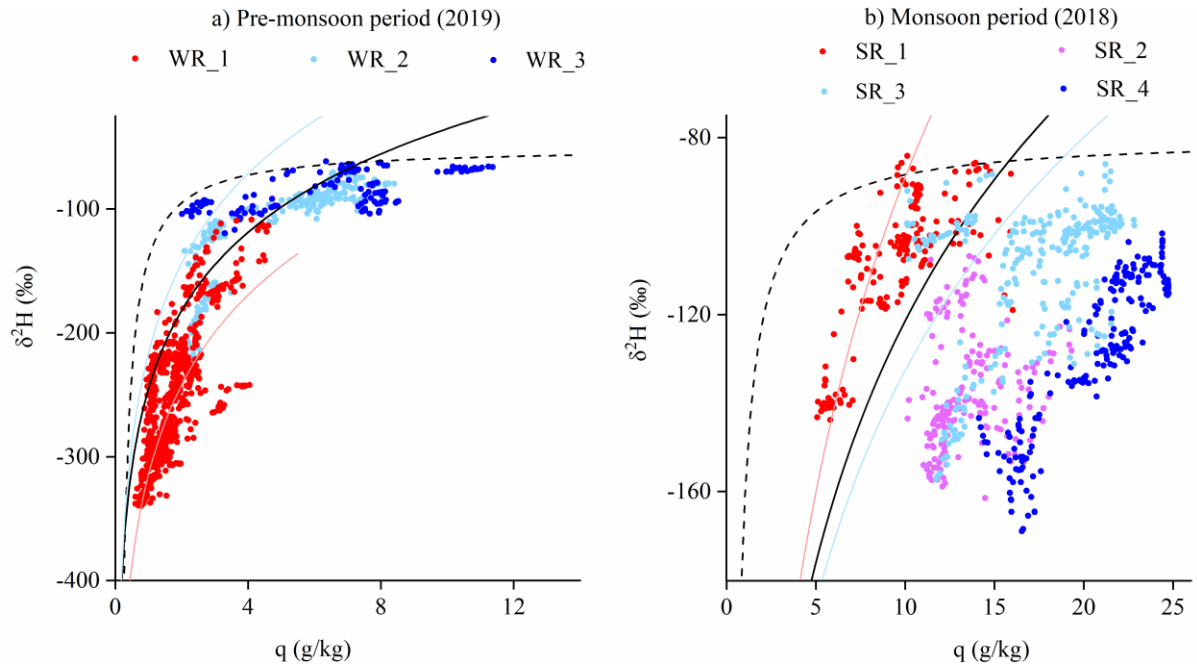
522
523   Fig.8 Scatterplot of observed vapor δ^2H (‰) versus specific humidity q (g/kg) during the pre-
524   monsoon period (a) and monsoon (b) period. The solid black curves show the Rayleigh
525   distillation line calculate for the initial conditions of δ^2H$_0$ = -50‰, T=15 °C during the pre-
526   monsoon period and δ^2H$_0$ = -80‰, T=25 °C during the monsoon period. The mixing lines
527   (dashed black curves) are calculated using a dry end-member with q = 0.2 g/kg and δ^2H = −
528   500 ‰ and air parcels for the corresponding Rayleigh curve as a wet end-member. The colored
529   solid curves show the uncertainty range of the Rayleigh curve, calculated for different initial
530   conditions of key moisture source regions: during March 2019, light red and light blue Rayleigh
531   curve are calculated for key moisture source regions of westerlies (δ^2H$_0$ = − 168.04‰, T=5°C)
532   and BoB (δ^2H$_0$= -77.37‰, T=26.46°C) separately in (a); during July-August 2018, light red
533   and light blue Rayleigh curve are calculated for key moisture source regions of westerlies
534   (δ^2H$_0$= -149.64‰, T=6.16°C) and BoB (δ^2H$_0$= -82.75‰, T=27.69°C) separately in (b). These
535   initial δ^2H are derived from Iso-GSM, the initial temperature and RH are derived from
536   NCAR/NCEP 2.5-deg global reanalysis data.

537

538   The progressive condensation of water vapor from an air parcel from the source region to
539   the sampling site and the subsequent removal of condensate results in a gradual reduction of
540   humidity and vapor isotope ratios. This relationship can be visualized in a q–δ diagram, which
541   has been used in many studies of the vapor isotopic composition (Noone, 2012;Galewsky et al.,
542   2016). Observations along the Rayleigh distillation line indicate progressive dehydration by
543   condensation. Observations above the Rayleigh line indicate either mixing between air masses
544   of contrasting humidity (Galewsky and Hurley, 2010) or evapotranspiration (Galewsky et al.,
545   2011;Samuels-Crow et al., 2015;Noone, 2012;Worden et al., 2007). Observations below the
546   Rayleigh line, even when considering the most depleted initial vapor conditions (light blue
547   Rayleigh curve in Fig 8b), indicate the influence of rain evaporation from depleted precipitation

548 (Noone, 2012;Worden et al., 2007). Figure 8 shows the observed vapor q–δ^2H for different
549 regions during the pre-monsoon (a) and monsoon (b) period. This figure will be interpreted in
550 the light of meteorological variables along back-trajectories (Fig.2).

551 During the pre-monsoon period, most q-δ^2H measurements are located surrounding or
552 overlapping the Rayleigh curve (the solid black curve in Fig.8a). Therefore, the observed spatial
553 pattern can mostly be explained by the gradual depletion of vapor isotopes by condensation.
554 The data for the three moisture sources are distributed in different positions of the Rayleigh
555 curve, relate to different moisture origins or different original vapor isotope values. This is
556 confirmed by the back-trajectory analysis: the Westerlies bring cold and dry air to northern
557 China (WR_1, Fig.3a, Fig.2a and c), consistent with the vapor further along the Rayleigh
558 distillation, and thus very depleted (Fig.5a). The observations in the WR_1 region (Fig.3c) are
559 closer to the q-δ^2H Rayleigh distillation curve calculated for the key moisture source regions of
560 westerlies, providing further evidence of the influence of water vapor source on vapor isotopes.
561 The relatively high T and q along the ocean-sourced air trajectory reaching southern China
562 (WR_3, Fig.3c, Fig.2a and c) is consistent with an early Rayleigh distillation phase during
563 moisture transport, and thus higher water vapor δ^{18}O in southern China (Fig.5a). Some
564 observations in the WR_3 region (Fig.3c) are located below the q-δ^2H Rayleigh distillation
565 curve, indicating the influence of rain evaporation (Noone, 2012;Worden et al., 2007). This is
566 consistent with the fact that air originates from the BoB, where deep convection begins to be
567 active, and thus rain evaporation become a source of water vapor.

568 During the monsoon period, we find a scattered relationship in the q–δ^2H diagram for
569 different regions, implying different moisture sources and/or water recycling patterns during
570 moisture transport. Data measured in the SR_1 region (Fig.3i) fall above the Rayleigh
571 distillation line (solid black curve in Fig.8b), likely due to the presence of moisture originating
572 from continental recycling. A larger number of q-δ^2H measurements (most of the measurements
573 from the SR_2, SR_3, and SR_4 regions, Fig.3i) are located below the Rayleigh curve,
574 indicating moisture originating from the evaporation of rain drops within and below convective
575 systems (Noone, 2012;Worden et al., 2007). In SR_3 and SR_4 regions, this is consistent with
576 the high precipitation rate along Southerly and Easterly back-trajectories (Fig.2f). The
577 convection is active over the Bay of Bengal, Pacific Ocean and South-Eastern Asia, as shown
578 by the low OLR (<240W/m 2) in these regions (Fig.S3) (Wang and Xu, 1997). Therefore, a
579 significant fraction of the water vapor originates from the evaporation of rain drops in
580 convective systems. These results support recent studies showing that convective activity
581 depleted the vapor during transport by the Indian and East Asian monsoon flow (Cai et al.,
582 2018;He et al., 2015;Gao et al., 2013). In SR_2 region, the relatively low water vapor δ^{18}O,
583 below the Rayleigh curve, is also probably associated with the evaporation of rain drop under
584 deep convective systems. This is confirmed by the high precipitation rates along Northerly
585 back-trajectories (Fig.2f), reflecting summer continental convection.

586 In northern China, q–δ diagrams show stronger distillation during the pre-monsoon period.
587 This suggests a "temperature dominated" control. Very low regional T during the pre-monsoon
588 period (Fig.S2 a and Fig.2a) are associated with low saturation vapor pressures and enhanced
589 distillation, producing lower vapor δ^{18}O. The T in summer is higher (Fig.S2 b and Fig.2b),
590 allowing for higher vapor δ^{18}O. The δ^{18}O$_{monsoon}$ - δ^{18}O$_{pre-monsoon}$ values in this region are therefore
591 positive (Fig.7a). In the South, q–δ diagrams suggest the stronger influence of rain evaporation

during the monsoon period. Higher precipitation amount significantly reduce $\delta^{18}O$ in the South (Fig.2f), even though T was higher during the monsoon period than in pre-monsoon. This suggests a "precipitation dominated" control in this region, explaining the negative values of $\delta^{18}O_{monsoon}$ - $\delta^{18}O_{pre-monsoon}$. This seasonal pattern in $\delta^{18}O$ is consistent with the results in precipitation isotopes (Araguás-Araguás et al., 1998;Wang and Wang, 2001). The boundary line separating the seasonal variations of $\delta^{18}O$ is also consistent with previous study on seasonal difference in vapor δ^2H retrieved by TES and GOSAT (Shi et al., 2020).

4.2 The $\delta^{18}O$-δ^2H relationship
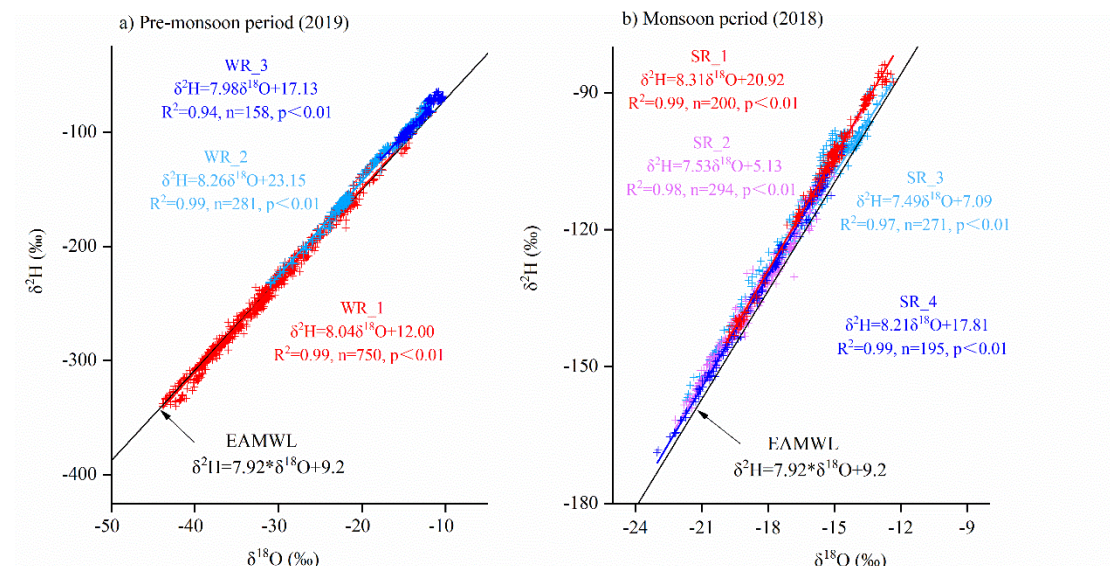
Fig.9 Regional patterns of vapor $\delta^{18}O$ - δ^2H relation during pre-monsoon period (a) and monsoon (b) period, compared with the East Asia Meteoric Water Line (EAMWL) (Araguás-Araguás et al., 1998).

The $\delta^{18}O$-δ^2H relationship is usually applied to diagnose the moisture source and water cycling processes related to evaporation. Figure 9 and Table 1 show the $\delta^{18}O$-δ^2H relationship for different regions in the two seasons. We also plot the East Asian Meteoric Water Line (EAMWL) for a reference. Vapor $\delta^{18}O$-δ^2H is usually located above Meteoric Water Line owing to the liquid water and vapor fractionation.

During the pre-monsoon period (Fig.9a), the data in northern China (WR_1, Fig.3a) are located at the lower-left area in the $\delta^{18}O$-δ^2H graph, with similar slope and intercept as EAMWL ($\delta^2H = 8.04 \delta^{18}O + 12.00$). This corresponds to air brought by the Westerlies and following Rayleigh distillation. The linear relationship for the vapor in middle China (WR_2, Fig.3b) has the steepest slope and highest intercept ($\delta^2H = 8.26\delta^{18}O + 23.15$). These properties are associated with a high d-excess, consistent with strong continental recycling by evapotranspiration (Aemisegger et al., 2014). As continental recycling is known to enrich the water vapor (Salati et al., 1979) and is associated with high d-excess (Gat and Matsui, 1991;Winnick et al., 2014). The high intercept is further consistent with a correlation between $\delta^{18}O$ and d-excess, which can typically result from continental recycling (Putman et al., 2019). The data for vapor originating from the BoB (WR_3, Fig.3c) are located to the upper right of the EAMWL. Their regression correlation shows similar features ($\delta^2H = 7.98 \delta^{18}O + 17.13$) to

that of the monsoon season (with a slope of 8.21 and an intercept of 17.81). We find similar atmospheric conditions in the BoB (with the region marked as rectangle in Fig.3c and h) during the two observation periods, with T=26°C and RH=76% during pre-monsoon period and T=28°C and RH=78% during the monsoon period, suggesting that the BoB source may have similar signals on vapor δ^{18}O and δ^2H in both seasons. These observed vapor δ^{18}O-δ^2H patterns are consistent with the back-trajectory results indicating that the Westerlies persist in northern China during the pre-monsoon period, while moisture from the BoB has already reached southern China.

During the monsoon period (Fig.9b), the data in northwestern China (SR_1, Fig.3e) with continental moisture sources is located in the upper right of the graph but above the EAMWL, with the steepest slope and highest intercept for the linear δ^{18}O-δ^2H relationship (δ^2H = 8.31δ^{18}O +20.92). In contrast, the observations in southeastern China with BoB sources (SR_4, Fig.3h) are located in the lower left of the graph, with relatively lower intercept (δ^2H = 8.21δ^{18}O +17.81). This is the opposite pattern compared to the pre-monsoon season. The observations from the SR_3 region (Fig.3g) also have a low slope and low intercept (δ^2H = 7.49 δ^{18}O +7.09). This is consistent with the oceanic moisture from the Pacific Ocean. Also, these δ^{18}O-δ^2H data are located in the upper right of the graph with more scattered relation (with the lowest correlation coefficient), suggesting more diverse moisture sources. This is consistent with the mixing of water vapor from continental recycling and Pacific Ocean (Fig.3g). The observations in northeastern China (SR_2, Fig.3f) are located at the lower left of the graph, suggesting the influence of condensation along trajectories in northern Asia (Fig.2f). Compared to the SR_3 and SR_4 regions, the slope and intercept of the observations in SR_2 region are lower (δ^2H = 7.53δ^{18}O +5.13), reflecting different origins of moisture.

4.3 Relationship with local meteorological variables
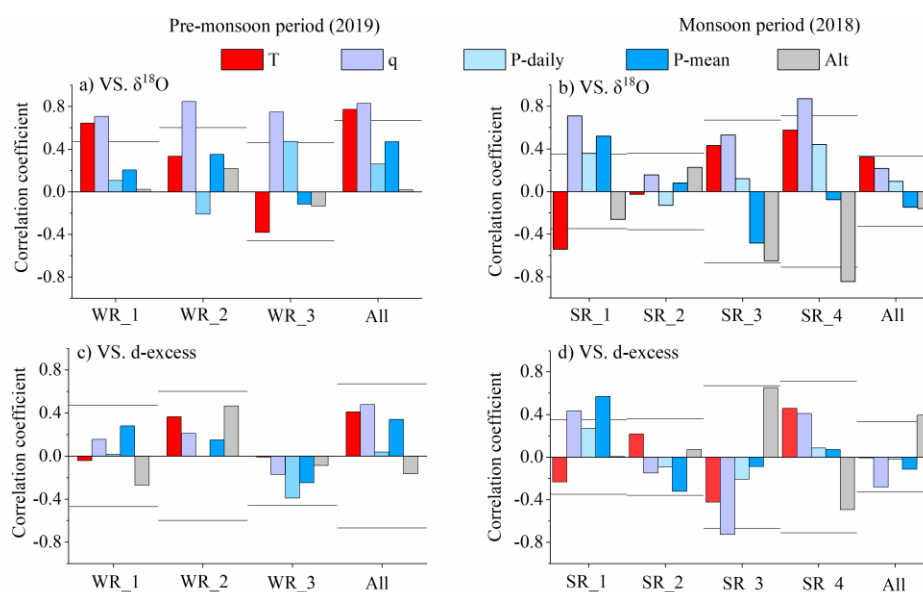
Fig.10 Regional patterns of the correlation between δ^{18}O (a, b), d-excess (c, d) and various local factors (temperature (T), specific humidity (q), daily precipitation amount (P-daily) and average precipitation amount over the entire observation period for each observation location   (P-

mean), and altitude (Alt)). The left panel is for the pre-monsoon period and the right is for the monsoon period. Horizontal lines indicate the correlation threshold for statistical significance ($p<0.05$), considered the degree of freedom.

Here we analyze the relationship between vapor $\delta^{18}O$, d-excess and local meteorological parameters, for all observations, and separately for the different regions (Fig.10 and Table S1).

We have taken particular care to estimate the statistical significance of the correlation coefficients. The statistical significance of a correlation depends on the correlation coefficient and on the degree of freedom D of the observed $\delta^{18}O$ and d-excess time series. Since these variables evolve smoothly in time and are sampled at a high frequency, the total number of samples overestimates the degree of freedom D of the time series. We thus estimated the degree of freedom D as $Ʈ/\eta$, where $Ʈ$ is the length of the sampling period and η is the characteristic auto-correlation time scale of the time series (an example of this calculation is given in III. Supplementary text). A similar method was used to calculate the degree of freedom of the signal in (Roca et al., 2010). Table S2 summarizes the threshold for the correlation coefficient to be statistically significant at 95%, for the two seasons, the different regions and the variable of interest.

During the pre-monsoon period, all observations taken together exhibit a "temperature effect" (the δ's decreasing with temperature, Dansgaard 1964) (Fig.10a), with significant and positive correlation between $\delta^{18}O$ and T ($r = 0.77$, $p<0.05$, Table S1). This results from the high correlation between $\delta^{18}O$ and q ($r = 0.83$, $p<0.05$, Table S1), consistent with the Rayleigh distillation, and between T and q ($r = 0.54$, $p<0.05$), consistent with the Clausius Clapeyron relationship. The vapor $\delta^{18}O$ in the WR_1 (Fig.3a) region show similar correlations with T and q as for all observations. Rayleigh distillation thus contributes to the relationship between $\delta^{18}O$ and T observed in northern China. In contrast, no significant positive correlation between vapor $\delta^{18}O$ and T is observed in the WR_3 region with the BoB water source. This is consistent with the fact that the moisture from the BoB has already influenced southern China during the pre-monsoon period (Fig.3c). The weak positive correlation in most regions between $\delta^{18}O$ and P-daily and P-mean might simply reflect the control of q on observed vapor $\delta^{18}O$, due to the relatively high correlation between observed P-mean and q, with $r = 0.58$ for all observations (Fig.4).

During the monsoon period (Fig 10b), no significant correlation emerges when considering all observations. Vapor $\delta^{18}O$ is still significantly correlated with q in the SR_1 (Fig.3e, $r = 0.71$, $p<0.05$, Table S1) and SR_4 (Fig.3h, $r = 0.87$, $p<0.05$, Table S1) regions. This is consistent with different degree of rain-out. This may reflect the synoptic-scale variations of convection. The absence of correlation with T suggests that the variations in q mainly reflect variations in relative humidity that are associated with different air mass origins or rain evaporation. The $\delta^{18}O$ is significantly anti-correlated with Alt in the SR_4 region ($r = -0.85$, $p<0.05$, Table S1), consistent with the "altitude effect" (the heavy isotope concentrations in fresh water decreasing with increasing altitude) in precipitation and water vapor (Dansgaard, 1964;Galewsky et al., 2016).

The vapor d-excess for all observations during the monsoon period (Fig.10d) is positively correlated with Alt ($r = 0.39$, $p<0.05$, Table S1). One possible reason is that the vapor d-excess is lower in coastal areas at lower altitudes, while at higher altitudes in the west, more continental

694 recycling of moisture leads to higher d-excess(Aemisegger et al., 2014). The positive
695 correlation between d-excess and altitude is consistent with previous studies in region (Acharya
696 et al., 2020). In the SR_1 region (Fig.3e), in arid northwestern China, vapor d-excess is
697 positively correlated with q (r = 0.43, p<0.05, Table S1) and P-mean (r = 0.57, p<0.05, Table
698 S1) during the monsoon period, suggesting that rain evaporation may also contribute to high d-
699 excess (Kong and Pang, 2016). Other than these examples, the correlation coefficients between
700 the d-excess and T, q, P, and Alt are not significant (Fig.10c and d), indicating that the local
701 meteorological variables are not strongly related to vapor d-excess, as was reported in previous
702 studies for precipitation isotopes (Guo et al., 2017;Tian et al., 2003).

703 4.4 Relationship with meteorological variables along trajectories
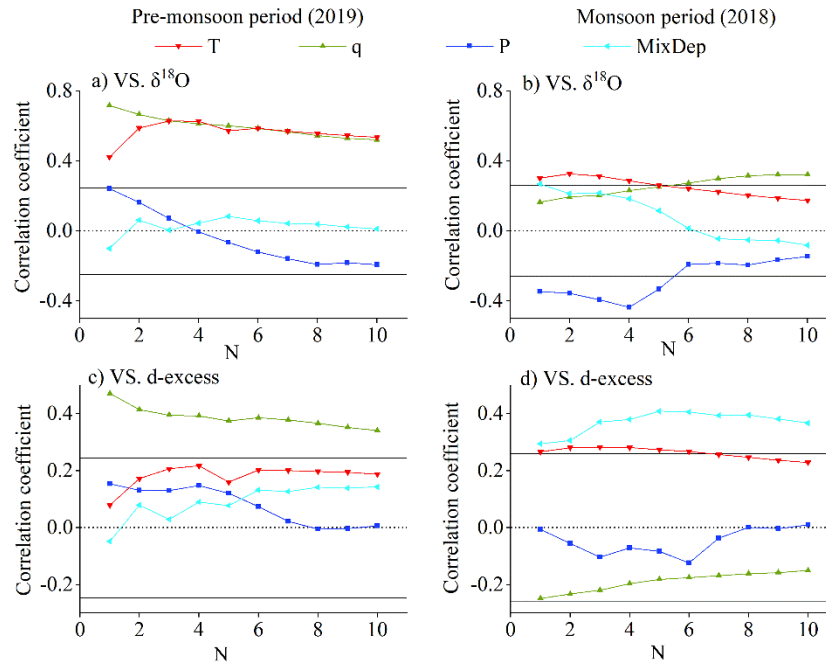
704
705 Fig.11 Correlation between $\delta^{18}O$ (a, b), d-excess (c, d)), and various meteorological factors (air
706 temperature (T), specific humidity (q), precipitation (P), and mixing depth (MixDep)) along the
707 air mass trajectories during the pre-monsoon period (the left panel) and monsoon period (the
708 right panel). The x-axis "N" represents the number of days prior to the observations (from 1
709 to 10 days). For example, when the number of days is 2, the correlations is calculated with the
710 temporal mean of meteorological data along the air mass trajectories during the 2days before
711 the observations. Horizontal solid lines indicate the correlation threshold for statistical
712 significance (p<0.05).

713
714   Reconstructions of paleoclimates using ice core isotopes have relied on relationships with
715 local temperatures, but many previous studies have suggested that water isotopes are driven by
716 remote processes along air mass trajectories. In particular, they emphasized the importance of
717 upstream convection in controlling the isotopic composition of water (Gao et al., 2013;He et
718 al., 2015;Vimeux et al., 2005, Cai and Tian, 2016). We therefore perform a correlation analysis
719 between vapor isotope observations and the temporal mean meteorological conditions along air
720 mass trajectories. The meteorological conditions are averaged over the previous days (N form

721 1 to 10) prior to the observations.

722 The $\delta^{18}O$ values have the strongest correlations with T and q along air mass trajectories
723 during the pre-monsoon period (Fig.11a). The results show gradually increasing positive
724 correlation coefficients as N changes from 10 to 3. This reflects the role of temperature and
725 humidity along air mass trajectories and the large spatial and temporal coherence of T variations
726 during the pre-monsoon period. During the monsoon period, the negative correlation
727 coefficients between $\delta^{18}O$ and P (Fig.11b) become more significant as N increases from 1 to 4
728 and less significant as N increases from 5 to 10. This result indicates a maximum impact of P
729 during a few days prior to the observations, as observed also for precipitation isotopes (Gao et
730 al., 2013;Risi et al., 2008a). It is further consistent with the influence of precipitation along
731 back-trajectories (Fig.2f). Mixing depth (MixDep) is stably and positively correlated with d-
732 excess. A hypothesis to explain this correlation is that when the MixDep is higher, stronger
733 vertical mixing of convective system transports vapor with higher d-excess values from higher
734 altitude to the surface (Galewsky et al., 2016;Salmon et al., 2019).

735 4.5 Relationship between water vapor isotopes and moisture sources

736 In section 4.1 to 4.4, we have discussed that different moisture sources and corresponding
737 processes on transport pathways are related to the observed spatial patterns both in vapor $\delta^{18}O$
738 and d-excess.

739 We also identify different isotopic values of vapor from different ocean sources during the
740 monsoon period. The vapor $\delta^{18}O$ in the zone from Beijing to Harbin and western China with
741 Pacific Ocean and continental origins (SR_3 region, about -17‰ to -13‰) are higher than those
742 in the Southeast with BoB sources (SR_4 region, about -23‰ to -15‰) (Fig.3i and Fig.5b). In
743 sections 4.1 and 4.2, we have shown that it is related to the extent of the Rayleigh distillation
744 and rain evaporation associated with convection along trajectories. Earlier studies suggest that
745 lower $\delta^{18}O$ values were observed from the Indian monsoon source than from Pacific Asian
746 monsoon moisture due to the different original isotope values in the source regions (Araguás-
747 Araguás et al., 1998). To better isolate the direct effect of moisture sources, we extract the initial
748 vapor isotopes of the Indian and East Asian monsoon systems (the regions are marked as
749 annotated rectangles in Fig.3g and h) for the sampling dates of 2018 from the Iso-GSM model.
750 The values are about $\delta^{18}O$=-12‰ and δ^2H =-83‰ in the northern BoB and $\delta^{18}O$ =-14‰ and
751 δ^2H =-97‰ in the eastern Pacific Ocean. The initial vapor isotope values of the two vapor
752 sources are not significantly different. The initial vapor isotopes in the BoB are even slightly
753 higher than those in the Pacific Ocean, contrary to moisture source hypothesis. The OLR was
754 significantly lower in the BoB than in the Pacific Ocean (Fig.S3). This suggests that the deeper
755 convection in the Indian Ocean leads to lower water vapor isotope ratios (Liebmann and Smith,
756 1996;Bony et al., 2008;Risi et al., 2008b;Risi et al., 2008a) in southeastern China, rather than
757 the initial composition of the moisture source.

758 Continental recycling probably also contribute to higher $\delta^{18}O$ in the SR_3 region (Fig.3i
759 and Fig.5b) (Salati et al., 1979), especially in western China (Fig.3i), which can be confirmed
760 by the higher d-excess in this region (Fig.5d) (Gat and Matsui, 1991;Winnick et al., 2014).
761 Except SR_3 region, continental recycling also has a strong influence on isotopes in the WR2
762 and SR1 regions, which suggested by the high values of $\delta^{18}O$ and d-excess, back-trajectories,
763 the location on the q-δ diagram, and the higher slopes and intercepts of $\delta^{18}O$-δ^2H relationship.

764 In the opposite, in the zone from Beijing to Harbin (Fig.3i), greater proportion of water vapor
765 from Pacific sources than continental recycling and is in the early stage of Rayleigh distillation,
766 could result in high vapor $\delta^{18}O$ (Fig.5b) but relatively low d-excess (Fig.5d).
767 In previous studies, the d-excess has been interpreted as reflecting the moisture source and
768 evaporation conditions (Jouzel et al., 1997). During the pre-monsoon period, lower T and higher
769 RH over evaporative regions for the vapor transported by the Westerlies (Fig.2a and g, Fig.S2
770 a and g) reduces the non-equilibrium fractionation at the moisture source and produces lower
771 vapor d-excess in the WR_1 region (Fig.3a, Fig.5c) (Jouzel et al., 1997;Merlivat and Jouzel,
772 1979). In contrast, higher T and lower RH over evaporative regions (Fig.2 a and g, Fig.S2 a and
773 g) for the vapor coming from the South leads to higher d-excess in southern China (WR_3,
774 Fig.3c, Fig.5c). This is consistent with the global-scale poleward decrease in T and increase in
775 surface RH over the oceans (despite the occurrence of very low RH at the sea ice edge during
776 cold air outbreaks (Thurnherr et al., 2020;Aemisegger and Papritz, 2018)), resulting in global-
777 scale poleward decrease in d-excess at mid-latitudes (Risi et al., 2013a;Bowen and Revenaugh,
778 2003). Alternatively, the low d-excess during the night over the continent in Northern China
779 during the pre-monsoon could also have contributions (Li et al., 2021). During the monsoon
780 period, the lower vapor d-excess observed in eastern China (Fig.5d) is likely a sign of the
781 oceanic moisture, derived from source regions where RH at the surface is high (Fig.2h and
782 Fig.S2 h) and thus reduce non-equilibrium fractionation and lower d-excess. The high d-excess
783 values observed in western and northwestern China (Fig.5d) reflect the influence of continental
784 recycling (Fig.3e and g).
785 The seasonal variation of moisture sources also results in a seasonal difference in d-excess
786 (Fig.8b). In southeastern China, RH over the ocean surface in summer is higher than in winter
787 (Fig.S2 g and h, and Fig.2g and h), resulting in negative values of d-excess$_{monsoon}$ - d-excess$_{pre-}$
788 $_{monsoon}$ (Fig.8b). Northwestern China has an opposite pattern of seasonal vapor d-excess. This
789 result largely due to the extremely low vapor d-excess during the pre-monsoon period (Fig.5c).
790 Also, we speculate that a greater contribution of continental recycling leads to higher d-excess
791 during the monsoon period than during the pre-monsoon period (Risi et al., 2013b) and the
792 positive values of the d-excess$_{monsoon}$ - d-excess$_{pre-monsoon}$ (Fig.8b).

793 4.6 Possible reasons for the biases in Iso-GSM

794 In section 3.3, we showed that Iso-GSM captured the isotopic variations during the pre-
795 monsoon season better than during the monsoon season. We hypothesize that this mainly could
796 be due to the larger contribution of synoptic-scale variations to the observed variations during
797 the monsoon season. Iso-GSM performs well during the pre-monsoon season, when seasonal
798 mean spatial variability dominates q and isotope. In contrast, it performs less well during the
799 monsoon season, when isotopic variations are significantly influenced by the synoptic-scale
800 variability. Among the synoptic influences, tropical cyclones, the Northern Summer Intra-
801 Seasonal Oscillation (BSISO) and local processes probably played a role. For example, during
802 our monsoon observations, landfall of tropical cyclones Jongdari and Yagi correspond to the
803 low values of $\delta^{18}O$ we observed in the eastern China (Fig.S7a). Bebinca corresponds to the low
804 values of $\delta^{18}O$ we observed in the southwestern China (Fig.S7a). Typhoons are known to be
805 associated with depleted rain and vapor (Bhattacharya et al., 2022;Gedzelman, 2003). Three
806 Northern Summer Intra-Seasonal Oscillation (BSISO) events occurred in China during about

807 July 28 - 31, August 5 - 8th and August 14 – 16 (Fig S8). The northward propagation of the
808 BSISO is associated with strong convection (Kikuchi, 2021) (Fig. S8). Moreover, short-lived
809 convective events that frequently occurred during our observation period (Wang et al., 2018).
810 It is possible that these rapid high-frequency synoptic events are not fully captured by Iso-GSM.
811 We expect that Iso-GSM captures the large-scale circulation. Yet, we notice that Iso-GSM
812 underestimates the depletion associated with tropical cyclones (Fig. 12b). We hypothesize that
813 given its coarse resolution, it underestimates the depletion associated with the meso-scale
814 structure. This might contribute to the overestimation of vapor $\delta^{18}O$ in southeastern China
815 (Fig.12b). In Northwestern China, Iso-GSM underestimates vapor $\delta^{18}O$, but also underestimates
816 precipitation, q and T (Fig.12b, d, f and h, Fig. S4). It is possible that Iso-GSM underestimates
817 the latitudinal extent of the monsoonal influence, which brings moist conditions, while
818 overestimating the influence of continental air, bringing dry conditions associated with depleted
819 vapor through Rayleigh distillation. It is also possible that Iso-GSM underestimates the
820 enriching effect of continental recycling. During the pre-monsoon period, Iso-GSM
821 overestimates the observed $\delta^{18}O$ along most of the survey route (Fig.12a), with the largest
822 difference in northwestern China, and underestimates the vapor $\delta^{18}O$ in the southern part of the
823 study region. Our results are consistent with previous studies showing that many models
824 underestimate the heavy isotope depletion in pre-monsoon seasons in subtropical and mid-
825 latitudes, especially in very dry regions (Risi et al., 2012). This was interpreted as overestimated
826 vertical mixing. The differences in $\delta^{18}O$ (Fig.12a) and q (Fig.12c) are spatially consistent. The
827 overestimation of $\delta^{18}O$ therefore could be due to the overestimation of q, and vice versa. These
828 biases could be associated with shortcomings in the representation of convection or in
829 continental recycling. Despite this, the good agreement during pre-monsoon period is probably
830 due to the dominant control by Rayleigh distillation on seasonal-mean spatial variations of
831 isotopes in this season, as concluded in the above. The q variation, in relation with T, drives
832 vapor isotope variations and is well captured by Iso-GSM spatially, with significant correlations
833 between observed and simulated q (r = 0.84, slope=0.70 in Table S3) and T (r = 0.87,
834 slope=0.70 in Table S3), though q is overestimated in the North and underestimated in the South.

835
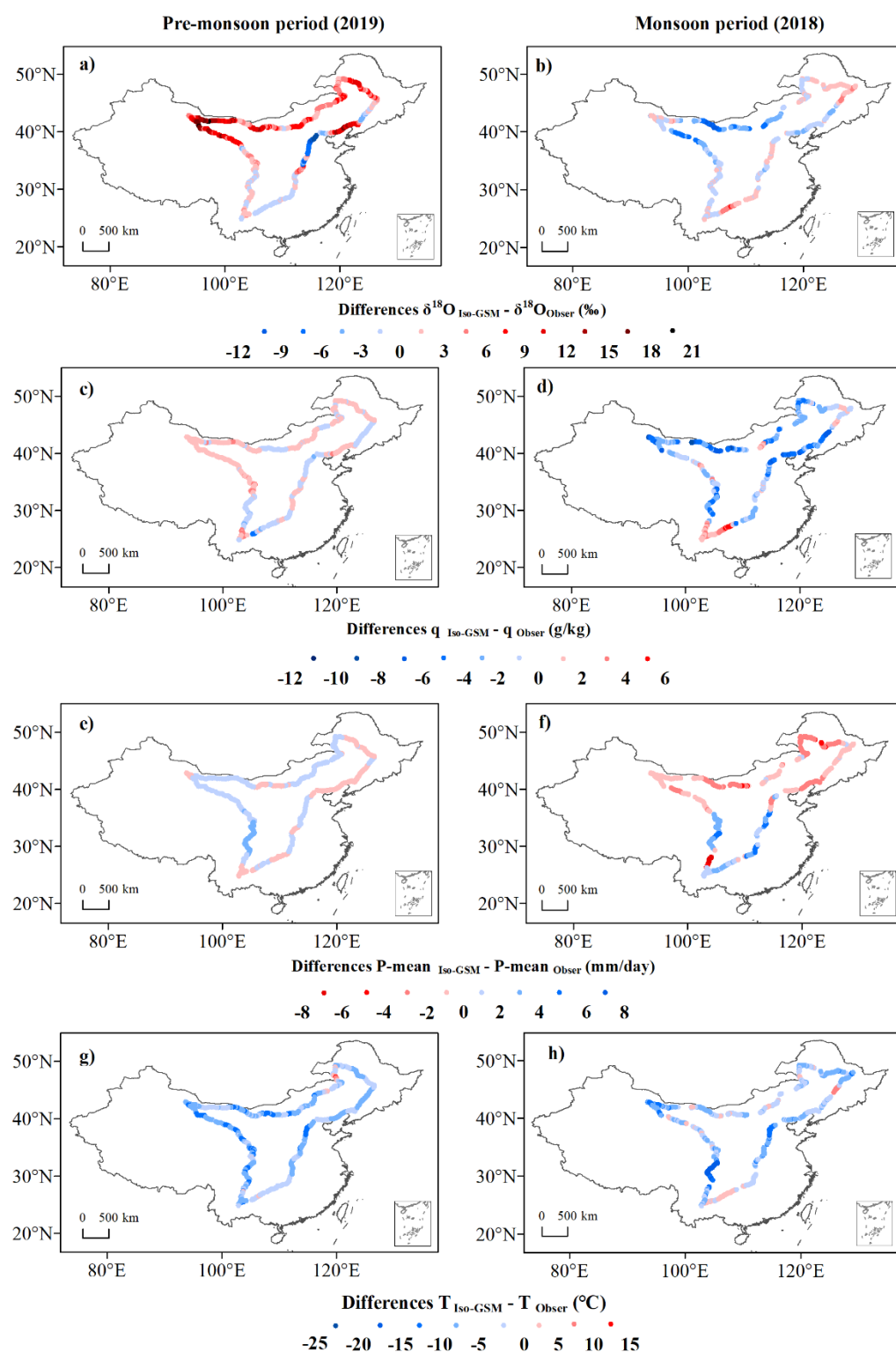
Fig.12 Spatial distribution of the differences between the outputs of Iso-GSM (subscripts are Iso-GSM) and observations (subscripts are Obser) during the pre-monsoon period (the left panel) and monsoon period (the right panel): $\delta^{18}O$ (a and b, ‰), specific humidity q (c and d, g/kg), P-mean for the sampling dates (e and f, mm/day), and temperature T (g and h, °C).

5 Conclusion

Our new, vehicle-based observations document spatial and seasonal variability in surface water vapor isotopic composition across a large part of China. Both during the pre-monsoon and monsoon periods, it is clear that different moisture sources and corresponding processes on transport pathways explain the spatial patterns both in vapor $\delta^{18}O$ and d-excess (summarized in Fig.13):

(1) During the pre-monsoon period (Fig.13a), the latitudinal gradient of vapor $\delta^{18}O$ and d-excess were observed. The gradient in $\delta^{18}O$ reflects the "temperature effect", Rayleigh distillation appears to be the dominant control, roughly consistent with earlier studies on precipitation. Vapor in northern China, derived from westerlies, and subject to stronger Rayleigh distillation (arrows fading from red to blue), is characterized by very low isotope ratios (blue shades). Less complete Rayleigh distillation (arrows fading from red to light red) results in less depleted vapor in southern China (light red shades). The vapor d-excess in northern China is low (green triangles series), probably due to the high RH over high-latitude oceanic moisture sources for the vapor transported by the Westerlies (green arrow), reducing the kinetic fractionation during ocean evaporation. In contrast, the lower RH over low-latitude moisture sources (yellow arrow) for the vapor transported to southern China leads to higher d-excess (yellow triangles series). Additional vapor sourced from continental recycling (orange twisted arrows), further increases the d-excess values in middle China. This distribution is consistent with the back-trajectory results showing that during the pre-monsoon period, the vapor in southwestern China comes from the BoB, whereas Westerly moisture sources still persist in northern China.

(2) During the monsoon period (Fig.13b), the lowest vapor $\delta^{18}O$ occurred in southwestern and northeastern China, and higher vapor $\delta^{18}O$ values were observed in between, while the d-excess features a west-east contrast. The relatively lower vapor $\delta^{18}O$ result from deep convection along the moisture transport pathway (blue clouds; arrows fading to blue). Meanwhile, the mixing with moisture from continental recycling (orange twisted arrows) increases the vapor $\delta^{18}O$ values in middle and northwestern China. We observed lower vapor $\delta^{18}O$ values when the moisture originates from the BoB than from the Pacific Ocean, consistent with stronger convection during transport. The dominance of oceanic-wet moisture (green arrows) results in the lower vapor d-excess (green triangles series) in eastern China, whereas continental recycling produces higher vapor d-excess in western and northwestern China (yellow triangles series).

(3) Variation in temperature drive the seasonal variations of vapor $\delta^{18}O$ in northern China, whereas convective activity along trajectories produces low vapor $\delta^{18}O$ curing the monsoon season and drive the seasonal variation in south China. Seasonal d-excess variation reflects different conditions in the sources of vapor: in southeastern China it is mainly due to differences in the RH over the adjacent ocean surface, while in northwestern China it is mainly due to the vapor transported by the Westerlies during the pre-monsoon period and a great contribution of continental recycling during the monsoon period.
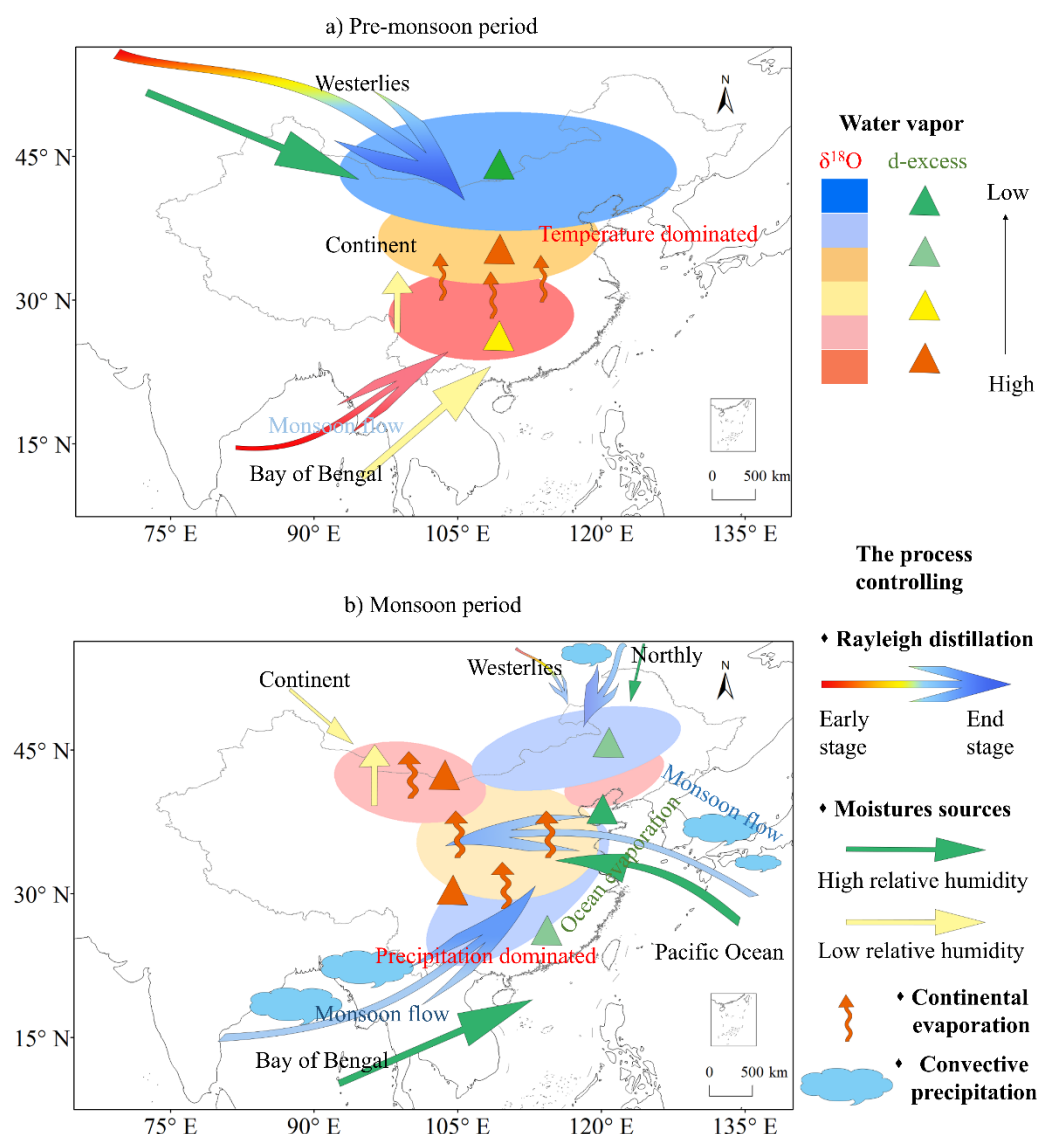
880
881 Fig.13 Schematic picture summarizing the different processes controlling the observed spatial
882 patterns and seasonality of vapor isotopes. Color gradient arrows from red to blue represent the
883 initial to subsequent extension of the Rayleigh distillation process along the water vapor
884 trajectory, corresponding to high to low values of δ18O; green arrows represent high relative
885 humidity and yellow arrows represent low relative humidity; orange twisted arrows represent
886 continental recycling; blue-sized clouds represent strong and weak convective processes; green
887 triangles series representing low values of d-excess; yellow triangles series representing high
888 values of d-excess.

889

890   Iso-GSM simulations and IASI satellite measurements indicate that during the pre-
891 monsoon period, the observed temporal variations along the route across China are mainly due
892 to multi-year seasonal-mean-spatial variations, and marginally due to synoptic-scale variations.
893 During the monsoon season, synoptic-scale and intra-seasonal variations might contribute
894 significantly to the apparent spatial patterns. However, since these variations have a smaller
895 amplitude than seasonal differences, the comparison of the two snapshots do provide a

896   representative picture of the climatological seasonal difference.

897   Our study on the processes governing water vapor isotopic composition at the regional
898 scale provides an overview of the spatial distribution and seasonal variability of water isotopes
899 and their controlling factors, providing an improved framework for interpreting the
900 paleoclimate proxy records of the hydrological cycle in low and mid-latitudes. In particular, our
901 results suggest a strong interaction between local factors and circulation, emphasizing the need
902 to interpret proxy records in the context of the regional system. This also suggests the potential
903 for changes in circulation to confound interpretations of proxy data.

904 **Data availability**

905 The data acquired during the field campaigns used can be accessed via the following link or
906 DOI: (1) Wang, Di; Tian, Lide (2022): Vehicle-based in-situ observations of the water vapor
907 isotopic composition across China during the monsoon season 2018. PANGAEA,
908 https://doi.org/10.1594/PANGAEA.947606; (2)Wang, Di; Tian, Lide (2022): Vehicle-based in-
909 situ observations of the water vapor isotopic composition across China during the pre-monsoon
910 season 2019. PANGAEA, https://doi.org/10.1594/PANGAEA.947627. . Other data used can be
911 downloaded from the corresponding website which were listed in the text.

912 **Author contributions**

913 L.T. and D.W. designed the research; D.W., and X.J. conducted to the field observations; J.C.
914 and J. B. contribute to the data calibration; Z.W. and K.Y performed Iso-GCM simulations;
915 D.W., C.R., and L.T. performed analysis; All authors contributed to the discussion of the results
916 and the final article; D.W. drafted the manuscript with contributions from all co-authors; C.R.,
917 L.T. and J. B. checked and modified the manuscript.

918 **Competing interests**

919 The authors declare that they have no conflict of interest.

920 **Acknowledgments**

921   The authors gratefully acknowledge NCAR/NCEP, GPCP and NOAA for provision of
922 regional and large-scale meteorological data. We are grateful to the NOAA Air Resources
923 Laboratory (ARL) that provided the HYSPLIT transport and dispersion model (http :/
924 /ready.arl .noaa .gov /HYSPLIT.php) and the HYSPLIT-compatible meteorological dataset
925 from GDAS. We thankfully acknowledge Yao Zhang, Xiaowen Zeng, Min Gan for technical
926 assistance. We thank Mingxing Tang and Ruoqun Zhang for partly participating in the field
927 observations. We thank to Zhaowei Jing for the discussions on Rayleigh distillation lines, and
928 thankfully acknowledge Yao Li, Zhongyin Cai and Rong Jiao for sharing some methods to use
929 Hysplit4 model. This work was supported by the Strategic Priority Research Program of
930 Chinese Academy of Sciences, Grant No. XDB40000000, the National Natural Science
931 Foundation of China (Grant 41771043, and 41701080), and Research Innovation Project for

932 Graduate Students of Yunnan University (Grant 2018Z098 and 2021Y040). Di Wang was
933 supported by the c.

934 **References**

935 Acharya, S., Yang, X., Yao, T., and Shrestha, D.: Stable isotopes of precipitation in Nepal Himalaya
936 highlight the topographic influence on moisture transport, Quaternary International, 565, 22-30, 2020.
937 Aemisegger, F., Pfahl, S., Sodemann, H., Lehner, I., Seneviratne, S. I., and Wernli, H.: Deuterium excess
938 as a proxy for continental moisture recycling and plant transpiration, Atmospheric Chemistry and
939 Physics, 14, 4029-4054, 2014.
940 Aemisegger, F., Spiegel, J., Pfahl, S., Sodemann, H., Eugster, W., and Wernli, H.: Isotope meteorology of
941 cold front passages: A case study combining observations and modeling, Geophysical Research Letters,
942 42, 5652-5660, 2015.
943 Aemisegger, F., and Papritz, L.: A climatology of strong large-scale ocean evaporation events. Part I:
944 Identification, global distribution, and associated climate conditions, Journal of Climate, 31, 7287-7312,
945 2018.
946 Aggarwal, P. K., Fröhlich, K., Kulkarni, K. M., and Gourcy, L. L.: Stable isotope evidence for moisture
947 sources in the asian summer monsoon under present and past climate regimes, Geophysical Research
948 Letters, 31, 239-261, 2004.
949 Araguás-Araguás, L., Froehlich, K., and Rozanski, K.: Stable isotope composition of precipitation over
950 southeast Asia, Journal of Geophysical Research: Atmospheres, 103, 28721-28742, 1998.
951 Bailey, A., Toohey, D., and Noone, D.: Characterizing moisture exchange between the Hawaiian
952 convective boundary layer and free troposphere using stable isotopes in water, Journal of Geophysical
953 Research: Atmospheres, 118, 8208-8221, 2013.
954 Benetti, M., Steen-Larsen, H. C., Reverdin, G., Sveinbjörnsdóttir, Á. E., Aloisi, G., Berkelhammer, M. B.,
955 Bourlès, B., Bourras, D., De Coetlogon, G., and Cosgrove, A.: Stable isotopes in the atmospheric marine
956 boundary layer water vapour over the Atlantic Ocean, 2012–2015, Scientific data, 4, 1-17, 2017.
957 Bhattacharya, S. K., Sarkar, A., and Liang, M. C.: Vapor isotope probing of typhoons invading the Taiwan
958 region in 2016, Journal of Geophysical Research: Atmospheres, 127, e2022JD036578, 2022.
959 Bonne, J.-L., Behrens, M., Meyer, H., Kipfstuhl, S., Rabe, B., Schönicke, L., Steen-Larsen, H. C., and Werner,
960 M.: Resolving the controls of water vapour isotopes in the Atlantic sector, Nature communications, 10,
961 1632, 2019.
962 Bony, S., Risi, C., and Vimeux, F.: Influence of convective processes on the isotopic composition (δ18O
963 and δD) of precipitation and water vapor in the tropics: 1. Radiative-convective equilibrium and Tropical
964 Ocean–Global Atmosphere–Coupled Ocean-Atmosphere Response Experiment (TOGA-COARE)
965 simulations, Journal of Geophysical Research: Atmospheres, 113, 2008.
966 Bowen, G. J., and Revenaugh, J.: Interpolating the isotopic composition of modern meteoric
967 precipitation, Water resources research, 39, 2003.
968 Bowen, G. J., Cai, Z., Fiorella, R. P., and Putman, A. L.: Isotopes in the Water Cycle: Regional-to Global-
969 Scale Patterns and Applications, Annual Review of Earth and Planetary Sciences, 47, 2019.
970 Brown, J., Simmonds, I., and Noone, D.: Modeling δ18O in tropical precipitation and the surface ocean
971 for present-day climate, Journal of Geophysical Research Atmospheres, 111, -, 2006.
972 Brubaker, K. L., Entekhabi, D., and Eagleson, P.: Estimation of continental precipitation recycling, Journal
973 of Climate, 6, 1077-1089, 1993.

Cai, Z., and Tian, L.: Processes governing water vapor isotope composition in the Indo-Pacific region: Convection and water vapor transport, Journal of Climate, 29, 8535-8546, 10.1175/JCLI-D-16-0297.1, 2016.

Cai, Z., Tian, L., and Bowen, G. J.: Spatial-seasonal patterns reveal large-scale atmospheric controls on Asian Monsoon precipitation water isotope ratios, Earth and Planetary Science Letters, 503, 158-169, 2018.

Dansgaard, W.: Stable isotopes in precipitation, Tellus, 16, 436-468, 1964.

Domrös, M., and Peng, G.: The climate of China, Springer Science & Business Media, 2012.

Fiorella, R. P., Bares, R., Lin, J. C., Ehleringer, J. R., and Bowen, G. J.: Detection and variability of combustion-derived vapor in an urban basin, Atmospheric Chemistry and Physics, 18, 8529-8547, 2018.

Fiorella, R. P., Bares, R., Lin, J. C., and Bowen, G. J.: Wintertime decoupling of urban valley and rural ridge hydrological processes revealed through stable water isotopes, Atmospheric environment, 213, 337-348, 2019.

Galewsky, J., and Hurley, J. V.: An advection-condensation model for subtropical water vapor isotopic ratios, Journal of Geophysical Research Atmospheres, 115, 2010.

Galewsky, J., Rella, C., Sharp, Z., Samuels, K., and Ward, D.: Surface measurements of upper tropospheric water vapor isotopic composition on the Chajnantor Plateau, Chile, Geophysical Research Letters, 38, 198-205, 2011.

Galewsky, J., Steen-Larsen, H. C., Field, R. D., Worden, J., Risi, C., and Schneider, M.: Stable isotopes in atmospheric water vapor and applications to the hydrologic cycle, Reviews of Geophysics, 54, 2016.

Gao, J., MassonDelmotte, V., Risi, C., He, Y., and Yao, T.: What controls precipitation $\delta18O$ in the southern Tibetan Plateau at seasonal and intra-seasonal scales? A case study at Lhasa and Nyalam, Tellus B, 65, 2013.

Gat, J. R., and Matsui, E.: Atmospheric water balance in the Amazon Basin: an isotopic evapotranspiration model, Journal of Geophysical Research: Atmospheres, 96, 13179-13188, 1991.

Gat, J. R.: Oxygen and hydrogen isotopes in the hydrologic cycle, Annual Review of Earth and Planetary Sciences, 24, 225-262, 1996.

Gedzelman, S.: Probing hurricanes with stable isotopes of rain and water vapor, Monthly Weather Review, 131, 1112-1127, 2003.

Gorski, G., Strong, C., Good, S. P., Bares, R., Ehleringer, J. R., and Bowen, G. J.: Vapor hydrogen and oxygen isotopes reflect water of combustion in the urban atmosphere, Proceedings of the National Academy of Sciences, 112, 3247-3252, 2015.

Gralher, B., Herbstritt, B., Weiler, M., Wassenaar, L. I., and Stumpp, C.: Correcting laser-based water stable isotope readings biased by carrier gas changes, Environmental science & technology, 50, 7074-7081, 2016.

Guo, X., Tian, L., Wen, R., Yu, W., and Qu, D.: Controls of precipitation $\delta 18 O$ on the northwestern Tibetan Plateau: A case study at Ngari station, Atmospheric Research, 189, 141-151, 2017.

He, Y., Risi, C., Gao, J., Masson-Delmotte, V., Yao, T., Lai, C. T., Ding, Y., Worden, J., Frankenberg, C., and Chepfer, H.: Impact of atmospheric convection on south Tibet summer precipitation isotopologue composition using a combination of in situ measurements, satellite data, and atmospheric general circulation modeling, Journal of Geophysical Research Atmospheres, 120, 3852-3871, 2015.

Hou, J., Huang, Y., Oswald, W. W., Foster, D. R., and Shuman, B.: Centennial-scale compound-specific hydrogen isotope record of Pleistocene–Holocene climate transition from southern New England, Geophysical Research Letters, 34, 2007.

1018 JingfengLiu,   CundeXiao,   MinghuDing,   and   JiawenRen:

1019 Variationsinstablehydrogenandoxygenisotopesinatmosphericwatervaporinthemarineboundarylayeracr

1020 ossawidelatituderange, Journal of Environmental Sciences, 26, 2266-2276, 2014.

1021 Johnson, J. E., and Rella, C. W.: Effects of variation in background mixing ratios of N 2, O 2, and Ar on

1022 the measurement of δ 18 O–H 2 O and δ 2 H–H 2 O values by cavity ring-down spectroscopy,

1023 Atmospheric Measurement Techniques, 10, 3073-3091, 2017.

1024 Johnson, K. R., and Ingram, B. L.: Spatial and temporal variability in the stable isotope systematics of

1025 modern precipitation in China: implications for paleoclimate reconstructions, Earth and Planetary

1026 Science Letters, 220, 365-377, 2004.

1027 Jouzel, J., Alley, R., Cuffey, K., Dansgaard, W., Grootes, P., Hoffmann, G., Johnsen, S., Koster, R., Peel, D.,

1028 and Shuman, C.: Validity of the temperature reconstruction from water isotopes in ice cores, Journal of

1029 Geophysical Research: Oceans, 102, 26471-26487, 1997.

1030 Khaykin, S. M., Moyer, E., Krämer, M., Clouser, B., Bucci, S., Legras, B., Lykov, A., Afchine, A., Cairo, F.,

1031 and Formanyuk, I.: Persistence of moist plumes from overshooting convection in the Asian monsoon

1032 anticyclone, Atmospheric Chemistry and Physics, 22, 3169-3189, 2022.

1033 Kikuchi, K.: The boreal summer intraseasonal oscillation (BSISO): A review, Journal of the Meteorological

1034 Society of Japan. Ser. II, 2021.

1035 Klein, E. S., Cherry, J., Young, J., Noone, D., Leffler, A., and Welker, J.: Arctic cyclone water vapor isotopes

1036 support past sea ice retreat recorded in Greenland ice, Scientific reports, 5, 10295, 2015.

1037 Kong, Y., and Pang, Z.: A positive altitude gradient of isotopes in the precipitation over the Tianshan

1038 Mountains: Effects of moisture recycling and sub-cloud evaporation, Journal of Hydrology, 542, 222-230,

1039 2016.

1040 Kurita, N.: Origin of Arctic water vapor during the ice-growth season, Geophysical Research Letters, 38,

1041 2011.

1042 Li, Y., An, W., Pang, H., Wu, S. Y., Tang, Y., Zhang, W., and Hou, S.: Variations of Stable Isotopic

1043 Composition in Atmospheric Water Vapor and their Controlling Factors—A 6-Year Continuous Sampling

1044 Study in Nanjing, Eastern China, Journal of Geophysical Research Atmospheres, 125, 2020.

1045 Li, Y., Aemisegger, F., Riedl, A., Buchmann, N., and Eugster, W.: The role of dew and radiation fog inputs

1046 in the local water cycling of a temperate grassland during dry spells in central Europe, Hydrology and

1047 Earth System Sciences, 25, 2617-2648, 2021.

1048 Liebmann, B., and Smith, C. A.: Description of a complete (interpolated) outgoing longwave radiation

1049 dataset, Bulletin of the American Meteorological Society, 77, 1275-1277, 1996.

1050 Linsley, B., Wellington, G., Schrag, D., Ren, L., Salinger, M., and Tudhope, A.: Geochemical evidence from

1051 corals for changes in the amplitude and spatial pattern of South Pacific interdecadal climate variability

1052 over the last 300 years, Climate Dynamics, 22, 1-11, 2004.

1053 Linsley, B. K., Zhang, P., Kaplan, A., Howe, S. S., and Wellington, G. M.: Interdecadal-decadal climate

1054 variability from multicoral oxygen isotope records in the South Pacific Convergence Zone region since

1055 1650 AD, Paleoceanography, 23, 2008.

1056 Liu, J., Song, X., Yuan, G., Sun, X., and Yang, L.: Stable isotopic compositions of precipitation in China,

1057 Tellus B: Chemical and Physical Meteorology, 66, 22567, 2014.

1058 Liu, Y., Cobb, K. M., Song, H., Li, Q., Li, C.-Y., Nakatsuka, T., An, Z., Zhou, W., Cai, Q., and Li, J.: Recent

1059 enhancement of central Pacific El Niño variability relative to last eight centuries, Nature

1060 communications, 8, 15386, 2017.

1061 McKinney, C. R., McCrea, J. M., Epstein, S., Allen, H., and Urey, H. C.: Improvements in mass

spectrometers for the measurement of small differences in isotope abundance ratios, Review of Scientific Instruments, 21, 724-730, 1950.

Mei'e, R., Renzhang, Y., and Haosheng, B.: An outline of China's physical geography, 1985.

Merlivat, L., and Jouzel, J.: Global climatic interpretation of the deuterium-oxygen 18 relationship for precipitation, Journal of Geophysical Research: Oceans, 84, 5029-5033, 1979.

Noone, D.: The influence of midlatitude and tropical overturning circulation on the isotopic composition of atmospheric water vapor and Antarctic precipitation, Journal of Geophysical Research: Atmospheres, 113, 2008.

Noone, D.: Pairing Measurements of the Water Vapor Isotope Ratio with Humidity to Deduce Atmospheric Moistening and Dehydration in the Tropical Midtroposphere, Journal of Climate, 25, 4476-4494, 2012.

Pausata, F. S. R., Battisti, D. S., Nisancioglu, K. H., and Bitz, C. M.: Chinese stalagmite delta O-18 controlled by changes in the Indian monsoon during a simulated Heinrich event, Nature Geoscience, 4, 474-480, 10.1038/ngeo1169, 2011.

Pfahl, S., and Sodemann, H.: What controls deuterium excess in global precipitation?, Climate of the Past, 10, 771-781, 10.5194/cp-10-771-2014, 2014.

Putman, A. L., Fiorella, R. P., Bowen, G. J., and Cai, Z.: A global perspective on local meteoric water lines: Meta-analytic insight into fundamental controls and practical constraints, Water Resources Research, 55, 6896-6910, 2019.

Risi, C., Bony, S., and Vimeux, F.: Influence of convective processes on the isotopic composition ($\delta 18O$ and δD) of precipitation and water vapor in the tropics: 2. Physical interpretation of the amount effect, Journal of Geophysical Research: Atmospheres, 113, -, 2008a.

Risi, C., Bony, S., Vimeux, F., Descroix, L., Ibrahim, B., Lebreton, E., Mamadou, I., and Sultan, B.: What controls the isotopic composition of the African monsoon precipitation? Insights from event-based precipitation collected during the 2006 AMMA field campaign, Geophysical Research Letters, 35, 851-854, 2008b.

Risi, C., Bony, S., Vimeux, F., and Jouzel, J.: Water-stable isotopes in the LMDZ4 general circulation model: Model evaluation for present-day and past climates and applications to climatic interpretations of tropical isotopic records, Journal of Geophysical Research-Atmospheres, 115, 10.1029/2009jd013255, 2010.

Risi, C., Noone, D., Worden, J., Frankenberg, C., Stiller, G., Kiefer, M., Funke, B., Walker, K., Bernath, P., Schneider, M., Wunch, D., Sherlock, V., Deutscher, N., Griffith, D., Wennberg, P. O., Strong, K., Smale, D., Mahieu, E., Barthlott, S., Hase, F., Garcia, O., Notholt, J., Warneke, T., Toon, G., Sayres, D., Bony, S., Lee, J., Brown, D., Uemura, R., and Sturm, C.: Process-evaluation of tropospheric humidity simulated by general circulation models using water vapor isotopologues: 1. Comparison between models and observations, Journal of Geophysical Research-Atmospheres, 117, 10.1029/2011jd016621, 2012.

Risi, C., Landais, A., Winkler, R., and Vimeux, F.: Can we determine what controls the spatio-temporal distribution of d-excess and 17 O-excess in precipitation using the LMDZ general circulation model?, Climate of the Past, 9, 2173-2193, 2013a.

Risi, C., Noone, D., Frankenberg, C., and Worden, J.: Role of continental recycling in intraseasonal variations of continental moisture as deduced from model simulations and water vapor isotopic measurements, Water Resources Research, 49, 4136-4156, 2013b.

Roca, R., Chambon, P., Jobard, I., Kirstetter, P.-E., Gosset, M., and Bergès, J. C.: Comparing satellite and surface rainfall products over West Africa at meteorologically relevant scales during the AMMA

campaign using error estimates, Journal of Applied Meteorology and Climatology, 49, 715-731, 2010.

Salati, E., Dall'Olio, A., Matsui, E., and Gat, J. R.: Recycling of water in the Amazon basin: an isotopic study, Water resources research, 15, 1250-1258, 1979.

Salmon, O. E., Welp, L. R., Baldwin, M. E., Hajny, K. D., Stirm, B. H., and Shepson, P. B.: Vertical profile observations of water vapor deuterium excess in the lower troposphere, Atmospheric Chemistry and Physics, 19, 11525-11543, 2019.

Samuels-Crow, K. E., Galewsky, J., Sharp, Z. D., and Dennis, K. J.: Deuterium excess in subtropical free troposphere water vapor: Continuous measurements from the Chajnantor Plateau, northern Chile, Geophysical Research Letters, 41, 8652-8659, 2015.

Sánchez-Murillo, R., Durán-Quesada, A. M., Esquivel-Hernández, G., Rojas-Cantillano, D., Birkel, C., Welsh, K., Sánchez-Llull, M., Alonso-Hernández, C. M., Tetzlaff, D., and Soulsby, C.: Deciphering key processes controlling rainfall isotopic variability during extreme tropical cyclones, Nature communications, 10, 1-10, 2019.

Saranya, P., Krishan, G., Rao, M., Kumar, S., and Kumar, B.: Controls on water vapor isotopes over Roorkee, India: Impact of convective activities and depression systems, Journal of Hydrology, 557, 679-687, 2018.

Schmidt, M., Maseyk, K., Lett, C., Biron, P., Richard, P., Bariac, T., and Seibt, U.: Concentration effects on laser-based $\delta 18O$ and $\delta 2H$ measurements and implications for the calibration of vapour measurements with liquid standards, Rapid Communications in Mass Spectrometry, 24, 3553-3561, 2010.

Schneider, D. P., and Noone, D. C.: Spatial covariance of water isotope records in a global network of ice cores spanning twentieth-century climate change, Journal of Geophysical Research: Atmospheres, 112, 2007.

Shi, X., Risi, C., Pu, T., Lacour, J. l., Kong, Y., Wang, K., He, Y., and Xia, D.: Variability of isotope composition of precipitation in the southeastern Tibetan Plateau from the synoptic to seasonal time scale, Journal of Geophysical Research: Atmospheres, 125, e2019JD031751, 2020.

Steen-Larsen, H. C., Johnsen, S., Masson-Delmotte, V., Stenni, B., Risi, C., Sodemann, H., Balslev-Clausen, D., Blunier, T., Dahl-Jensen, D., and Ellehøj, M. D.: Continuous monitoring of summer surface water vapor isotopic composition above the Greenland Ice Sheet, Atmospheric Chemistry and Physics, 13, 4815-4828, 2013.

Steen-Larsen, H. C., Risi, C., Werner, M., Yoshimura, K., and Masson-Delmotte, V.: Evaluating the skills of isotope-enabled General Circulation Models against in-situ atmospheric water vapor isotope observations, Journal of Geophysical Research, 122, 246-263, 2017.

Tan, M.: Circulation effect: response of precipitation delta O-18 to the ENSO cycle in monsoon regions of China, Climate Dynamics, 42, 1067-1077, 10.1007/s00382-013-1732-x, 2014.

Terzer-Wassmuth, S., Wassenaar, L. I., Welker, J. M., and Araguás-Araguás, L. J.: Improved high-resolution global and regionalized isoscapes of $\delta 18O$, $\delta 2H$ and d-excess in precipitation, Hydrological Processes, 35, e14254, 2021.

Thompson, L. G.: Ice core evidence for climate change in the Tropics: implications for our future, Quaternary Science Reviews, 19, 19-35, 10.1016/s0277-3791(99)00052-9, 2000.

Thompson, L. G., Yao, T., Mosley-Thompson, E., Davis, M., Henderson, K., and Lin, P.-N.: A high-resolution millennial record of the South Asian monsoon from Himalayan ice cores, Science, 289, 1916-1919, 2000.

Thompson, L. o., Mosley-Thompson, E., Davis, M., Lin, P., Yao, T., Dyurgerov, M., and Dai, J.: "Recent warming": ice core evidence from tropical ice cores with emphasis on Central Asia, Global and Planetary Change, 7, 145-156, 1993.

Thompson, L. o., Yao, T., Davis, M., Henderson, K., Mosley-Thompson, E., Lin, P.-N., Beer, J., Synal, H.-A., Cole-Dai, J., and Bolzan, J.: Tropical climate instability: The last glacial cycle from a Qinghai-Tibetan ice core, science, 276, 1821-1825, 1997.

Thurnherr, I., Kozachek, A., Graf, P., Weng, Y., Bolshiyanov, D., Landwehr, S., Pfahl, S., Schmale, J., Sodemann, H., and Steen-Larsen, H. C.: Meridional and vertical variations of the water vapour isotopic composition in the marine boundary layer over the Atlantic and Southern Ocean, Atmospheric Chemistry and Physics, 20, 5811-5835, 2020.

Tian, L., Yao, T., Schuster, P. F., White, J. W. C., Ichiyanagi, K., Pendall, E., Pu, J., and Yu, W.: Oxygen-18 concentrations in recent precipitation and ice cores on the Tibetan Plateau, Journal of Geophysical Research Atmospheres, 108, -, 2003.

Tian, L., Yao, T., Li, Z., MacClune, K., Wu, G., Xu, B., Li, Y., Lu, A., and Shen, Y.: Recent rapid warming trend revealed from the isotopic record in Muztagata ice core, eastern Pamirs, Journal of Geophysical Research: Atmospheres, 111, 2006.

Tian, L., Yao, T., MacClune, K., White, J. W. C., Schilla, A., Vaughn, B., Vachon, R., and Ichiyanagi, K.: Stable isotopic variations in west China: A consideration of moisture sources, Journal of Geophysical Research-Atmospheres, 112, 10.1029/2006jd007718, 2007.

Tian, L., Yu, W., Schuster, P. F., Wen, R., Cai, Z., Wang, D., Shao, L., Cui, J., and Guo, X.: Control of seasonal water vapor isotope variations at Lhasa, southern Tibetan Plateau, Journal of Hydrology, 580, 124237, 2020.

Van Breukelen, M., Vonhof, H., Hellstrom, J., Wester, W., and Kroon, D.: Fossil dripwater in stalagmites reveals Holocene temperature and rainfall variation in Amazonia, Earth and Planetary Science Letters, 275, 54-60, 2008.

Vuille, M., and Werner, M.: Stable isotopes in precipitation recording South American summer monsoon and ENSO variability: observations and model results, Climate Dynamics, 25, 401-413, 2005.

Wallace, J. M., and Hobbs, P. V.: Atmospheric science: an introductory survey, Elsevier, 2006.

Wang, B., and Xu, X.: Northern Hemisphere summer monsoon singularities and climatological intraseasonal oscillation, Journal of Climate, 10, 1071-1085, 1997.

Wang, B.: Rainy season of the Asian–Pacific summer monsoon, Journal of Climate, 15, 386-398, 2002.

Wang, D., and Wang, K.: Isotopes in precipitation in China (1986–1999), Science in China Series E: Technological Sciences, 44, 48-51, 2001.

Wang, G., Lan, H., and Liu, Z.: Stable isotope record of super typhoon Lekima (2019), Atmospheric Research, 264, 105822, 2021.

West, J. B., Bowen, G. J., Dawson, T. E., and Tu, K. P.: Isoscapes: understanding movement, pattern, and process on Earth through isotope mapping, Springer, 2009.

Winnick, M. J., Chamberlain, C. P., Caves, J. K., and Welker, J. M.: Quantifying the isotopic 'continental effect', Earth and Planetary Science Letters, 406, 123-133, 2014.

Worden, J., Noone, D., Bowman, K., and Tropospheric Emission, S.: Importance of rain evaporation and continental convection in the tropical water cycle, Nature, 445, 528-532, 10.1038/nature05508, 2007.

Wright, H. E.: Global climates since the last glacial maximum, U of Minnesota Press, 1993.

Yang, H., Johnson, K. R., Griffiths, M. L., and Yoshimura, K.: Interannual controls on oxygen isotope variability in Asian monsoon precipitation and implications for paleoclimate reconstructions, Journal of Geophysical Research Atmospheres, 121, 8410–8428, 2016.

Yao, T., Ding, L., Pu, J., Liu, J., and Yang, Z.: Characteristic of $\delta^{18}O$ in snow and its relation with moisture sources in Tanggula Mountains, Tibetan Plateau, Chinese Science Bulletin, 36, 1570-1573, 1991.

1194 Yoshimura, K., and Kanamitsu, M.: Specification of External Forcing for Regional Model Integrations,
1195 Mon.wea.rev, 137, 1409-1421, 2009.
1196 Zhao, L., Xiao, H., Zhou, M., Cheng, G., Wang, L., Yin, L., and Ren, J.: Factors controlling spatial and
1197 seasonal distributions of precipitation $\delta 18O$ in China, Hydrological Processes, 26, 143-152, 2012.
1198